Airway Epithelial SARS-CoV-2 Infectious and Repair Responses: Relationships to Age, Sex, and Post-COVID Pulmonary Syndromes

Hong Dang[1*], Caitlin E. Edwards[2*], Takafumi Kato[1,3*], Boris Reidel[1], Rita M. Meganck[4], Charles R. Esther, Jr[1]., Camille Ehre[1], M. Leslie Fulcher[1], Alexis B. Bailey[2], Michelle R. Cooley[5], Yu Mikami[1,6], Takanori Asakura[7], Padraig E. Hawkins[1], Minako Saito[1], Jeffrey L. Myers[8], Kristine Konopka[8], Firoozeh V Gerayeli[9], Hye Yun Park[9], Don D. Sin[9,10], Alessandra Livraghi-Butrico[1], Kenichi Okuda[1], Raymond J. Pickles[1,11], Sabra Klein[12], Scott H. Randell[1], Wanda K. O'Neal[1], Ralph S. Baric[2], Richard C. Boucher[1]

[1]Marsico Lung Institute/Cystic Fibrosis Research Center, School of Medicine, University of North Carolina at Chapel Hill, Chapel Hill, NC

[2]Department of Epidemiology, University of North Carolina at Chapel Hill, Chapel Hill, NC

[3]NHO Tokyo National Hospital, Tokyo, Japan

[4]Department of Molecular Microbiology, Washington University School of Medicine, St. Louis, MO, USA.

[5]The University of Chicago Medical Center

[6]Department of Respiratory Medicine, Graduate School of Medicine, the University of Tokyo, Tokyo, Japan, 113-8655

[7]Division of Pulmonary Medicine, Department of Medicine, Keio University School of Medicine, Tokyo, Japan

[8]Department of Pathology, University of Michigan Medical School, Ann Arbor, MI

[9]Centre for Heart Lung Innovation, St Paul's Hospital, Vancouver, BC, Canada

24 [10]Division of Respiratory Medicine, Department of Medicine, University of British Columbia,
25 Vancouver, BC, Canada
26 [11]Department of Microbiology and Immunology, University of North Carolina at Chapel Hill,
27 Chapel Hill, NC
28 [12]Bloomberg School of Public Health, Johns Hopkins University, Baltimore, MD
29
30 **Corresponding Author:**
31 Richard C. Boucher
32 7008 Marsico Hall
33 Chapel Hill, NC 27599-7248
34 919-966-7064
35 richard_boucher@med.unc.edu)
36
37 *contributed equally to this manuscript
38
39 **Conflict of Interest Statement:** Drs. Randell and O'Neal serve as grant reviewers for the Cystic
40 Fibrosis Foundation. Dr. Baric is a member of the advisory boards for VaxArt, Takeda and
41 Invivyd, has consulted for Gilead, and has collaborative projects with Gilead, J&J, and Hillevax,
42 focused on unrelated projects.
43

Abstract

The long-term pulmonary sequelae of SARS-CoV-2 respiratory infections reflect infection severity, innate and adaptive immunity, and respiratory epithelial repair. This study investigated the acute and reparative responses as a function of age and sex in primary human bronchial epithelial (HBE) cultures utilizing a 14-day SARS-CoV-2 infection protocol. SARS-CoV-2 infection peaked at 3 days post-infection (dpi) with an ~ 2 log titer suppression at 14 dpi. SARS-CoV-2 infection induced interferon, interferon-induced gene, and cell damage responses. No age- or sex-dependent effects on SARS-CoV-2 infection were detected. Airway epithelia repaired to an abnormal mucus metaplastic/inflammatory state that reflected potentially beneficial and adverse consequences at 14 dpi. Repair processes were infection severity-dependent, not sex-dependent, and were more robust in young donor cultures. Analyses of long-COVID subjects with persistent pulmonary fibrosis or persistent bronchitic airway diseases exhibited expression of HBE 14 dpi failed repair gene signatures, including ISG gene signatures. Human airway epithelial repair post-SARS-CoV-2 is prolonged and incomplete *in vitro* over 14 days, and persistently abnormal repair may contribute to phenotypes of people with long-COVID pulmonary syndrome.

Introduction

The respiratory outcomes following SARS-CoV-2 infections reflect multiple genetic and environmental variables (1-3). The severity of the lower airway infection, coupled with virus-modified epithelial repair programs and pre-existing epithelial health, are major variables predicting the severity of SARS-CoV-2 outcomes (4-8). Age and sex have also been related to SARS-CoV-2 disease severity (9-13). Children of both sexes are reported to exhibit less severe disease outcomes than adults (14, 15). Within the adult population, SARS-CoV-2 infection in older males generally is associated with more persistent disease (16). However, it has been difficult to attribute the relative risk of persistent disease in older males to differences in intrinsic epithelial infectivity/innate defense, age of the immune system, and/or comorbidities (17-20).

The first goal of this study was designed to identify potential contributions of human bronchial epithelia (HBE) to the acute and chronic (persistent COVID) outcomes of SARS-CoV-2 respiratory infections *in vitro* as a function of sex and age. Well-differentiated HBE cultures derived from sex-matched donors comprising a wide spectrum of age, including children aged 4 mo-8 yrs, young adults (20-30 yrs; referred to as mature), and the elderly (> 69 yrs), were studied over a prolonged post-SARS-CoV-2 inoculation (14 day interval) to capture potential age- and sex-dependent differences in: 1) the kinetics, magnitude and clearance of the initial infection; 2) the response/effects on the respiratory epithelium at peak viral infection; 3) how respiratory epithelia manifest SARS-CoV-2 infection post the peak infection period; and 4) how respiratory epithelia adapt and repair after peak epithelial infection/damage. A second goal of this study investigated whether *in vitro* d14-derived airway epithelial repair gene expression profiles persisted in specimens/data from subjects with prolonged (many months) failed epithelial repair

84 manifested in fibrotic and "bronchitic" sequelae of SARS-CoV-2 infection.

85

86 **Results**

87 **A. Global kinetics of virus infection**

88 ***Kinetics of Viral Titers***

89 Evidence of productive viral infection was present in 23 of the 24 experimental cultures of
90 human bronchial epithelial (HBE) cells as assayed by live virus titers outlined in Protocol 1
91 (**Figure 1A and Supplemental Figure 1A;** note, the absence of infection of the one culture was
92 deemed to reflect technical reasons, and it was removed from all analyses; see **Supplemental**
93 **Table 1**). Measurable increases in virus titer were observed at 1 day post-infection (dpi), and
94 titers peaked in 22/23 HBE donors at 3 dpi, the rate increasing with an average slope of 1.59 log
95 titer/day (**Figure 1A and Supplemental Figure 2Ai**). Titers were reduced by 7 dpi and either
96 leveled off or continued to decrease by 14 dpi, with 9 of 23 cultures exhibiting no measurable
97 live virus titer at 14 dpi (**Figure 1A**). Consequently, throughout this report, cultures that exhibit a
98 loss of live virus by 14 dpi are termed "suppressors" and those cultures with measurable titers
99 still present at 14 dpi are termed "non-suppressors". The slopes describing the decline of
100 infection over the 3-14 dpi interval described a viral clearance rate ~5 times slower than the rate
101 of virus production between 1-3 dpi (average slope of -0.3 log titer/day; **Supplemental Figure**
102 **2Aii**). The rate of decrease was faster (by -0.23 log titer/day) in suppressors vs. non-suppressor
103 HBE donors (**Supplemental Figure 2Aiii**). Collectively, the kinetics and magnitude of virus
104 growth observed *in vitro* resembled those of previous *in vitro* studies (21, 22) and *in vivo*
105 challenge studies of young healthy subjects (23).

106

107 ***Kinetics of Total Intracellular Viral Transcripts***

108 In addition to live virus titer determinations, intracellular viral RNA transcripts were measured at
109 time of culture collection by bulk RNA sequencing (bulk RNAseq). The nucleocapsid (N)
110 transcript was selected as an indicator of global SARS-CoV-2 viral mRNA and genome
111 production (see Supplemental methods for explanation) (24). N transcripts, expressed as
112 transcripts/million reads (TPM), were detectable by 1 dpi, increased to peak values at 3 dpi, and
113 then subsequently declined through 14 dpi (**Figure 1B**). The rate of acquisition of viral TPM was
114 similar to that measured by titer (slope 1.12 vs. 1.59, respectively; **Supplemental Figure 2, Bi**
115 **vs. Ai**). In contrast to the loss of detectable live virus titer in suppressors, a complete loss of
116 intracellular viral transcripts was not observed at 14 dpi in any HBE culture (compare **Figure 1,**
117 **A and B, and Supplemental Figure 2, Aii and Bii, Aiii and Biii**). These data demonstrate the
118 persistence of intracellular viral RNA in all cultures, despite the absence of measurable live virus
119 in 39% of the cultures.

120

121 ***Kinetics of HBE Apical Surface Viral Proteome***

122 Proteomics analyses identified SARS-CoV-2 viral proteins present in the apical washes sampled
123 across all dpi (**Figure 1C and Supplemental Figure 2C**). Nucleocapsid (NCAP) was at the
124 borderline of detection at 1 dpi, peaked at 3 dpi, and waned approximately 10-fold by 14 dpi
125 (**Figure 1C and Supplemental Figure 2C, i and ii**).While we focused on NCAP protein as
126 representative, similar patterns were observed for the spike protein, and, despite ~10-fold less
127 protein levels, for ORF8 (also called NS8) and ORF9B (**Supplemental Figure 2D**). As with
128 intracellular viral TPM, extracellular viral protein was still detectable at 14 dpi in suppressor
129 cultures (**Supplemental Figure 2Ciii**).

130

131 ***Correlations between Viral Titers, Intracellular TPM, and Apical Viral Proteins***

132 Globally, viral titers were correlated with both SARS-CoV-2 RNA expression (using N mRNA
133 as the representative transcript; **Figure 1Di**) and protein (using NCAP as the representative
134 SARS-CoV-2 protein; **Figure 1Dii**). The correlation was strongest between SARS-CoV-2 RNA
135 and NCAP protein (**Figure 1Diii**). The complete suppression of SARS-CoV-2 titers in cultures
136 that continued to exhibit measurable SARS-CoV-2 gene expression and extracellular protein
137 reduced the overall correlations with live virus titer. Comparisons of viral titer with SARS-CoV-
138 2 TPM or extracellular viral protein with time revealed a reduction in both viral:TPM or viral:N
139 protein from 1 dpi to 3 dpi, followed by a linear increase in ratios by 7 dpi, which leveled off in
140 non-suppressors at 14 dpi (**Figure 1E**). Overall, these findings suggest two conclusions: 1)
141 SARS-CoV-2 virus is maximally efficient at producing infectious virions in HBE cultures at 3
142 dpi, waning thereafter; and 2) a period of viral RNA persistence and protein shedding onto apical
143 HBE surfaces in the absence of detectable infectious virions can occur late (*e.g.*, 14 dpi) in a
144 SARS-CoV-2 infection, a finding of relevance to clinical antigen testing as a measure of
145 infectious virus (23, 25).

146

147 ***SARS-CoV-2 Mutation Analyses***

148 We tested the hypothesis that the mutation load in the SARS-CoV-2 genome would lead to the
149 ability of the virus to persist in human airway epithelial cultures. Mutations acquired by the
150 SARS-CoV-2 virus over 14 dpi were identified for each culture. Both coding and non-coding
151 mutations were observed throughout viral RNA at 14 dpi **(Supplemental Figure 2Ei**). There
152 were no differences in mutation load amongst cultures that suppressed or did not suppress viral

153 titers (**Supplemental Figure 2Eii**). Thus, we conclude that HBE responses, not viral mutations,
154 were the major drivers of viral kinetics in our system.
155
156 **B. Variables that affect HBE SARS-CoV-2 Infectivity**
157 The basal state of airway epithelia is a major contributor to viral infectivity (26). Accordingly,
158 we analyzed expression in 1 dpi mock exposed cultures for variables reportedly related to SARS-
159 CoV-2 viral infectivity referenced to SARS-CoV-2 titers at 3 dpi. As expected, mRNA
160 expression levels at 1 dpi in mock (basal) cultures for the proteins mediating SARS-CoV-2
161 binding/entry, *e.g.*, ACE2, TMPRSS2, and TMEM106B (27), were positively and significantly
162 correlated with SARS-CoV-2 titers at 3 dpi (**Figure 2A-C**). Multiple studies have also focused
163 on the relationships between ciliated cells and infection of airway epithelia by SARS-CoV-2 (22,
164 28-31). Two indices of HBE culture ciliation were utilized to examine relationships to infection:
165 1) The cilia-covered apical surface of the epithelium per basement membrane length was
166 morphologically scored in mock cultures paired with infected cultures; and 2) a gene set based
167 on cell ciliation was constructed and used to analyze mock 1 dpi cultures. The two metrics were
168 correlated (r^2=0.49; **Supplemental Figure 3A**), and positive but non-significant correlations
169 were observed between both metrics and viral titer 3 dpi (**Figure 2D and Supplemental Figure**
170 **3B).** The relationships observed between viral titers with ACE2, TMPRSS2, and ciliation were
171 generally similar when correlated to viral RNA (**Supplemental Figure 3C-E**).
172
173 We next evaluated whether baseline interferon expression, potentially reflecting a preexisting
174 inflammatory state, would associate with viral titer at 3 dpi (26, 32-34). The baseline expression
175 of a 13 gene index set of Type I interferon (IFN) stimulated genes previously reported, and with

176 mean expression >50 TPM from mock infection samples, was utilized for this analysis (35). No
177 relationships were detected between the basal expression of these genes and SARS-CoV-2
178 infection as indexed by viral titer or viral N gene TPM at 3 dpi (**Supplemental Figure 3F**). In
179 addition, an index of genes reported to govern viral entry/infectivity was developed and tested
180 for relationships to infectivity (36). A significant correlation was observed between basal
181 expression of these genes and SARS-CoV-2 titer and viral N at 3 dpi (**Figure 2E and**
182 **Supplemental Figure 3G)**. Curiously, many of these genes were also upregulated by virus in the
183 bulk RNAseq data (**Supplemental Figure 3H**). Finally, PLSCR1 has been reported to inhibit
184 SARS-CoV-2 entry/replication (37). In contrast to predictions, a positive correlation was
185 observed between mock/basal PLSCR1 expression and SARS-CoV-2 titer at 3 dpi (**Figure 2F)**.
186

187 **C. IFN and ISG Response Kinetics**

188 The interferon pathway is of critical importance in host responses to infection (26, 38-41). After
189 SARS-CoV-2 infection, HBE cultures robustly increased expression of *IFNL1*, *IFNL2*, *IFNL3*
190 and *IFNB1* (**Figure 3A**), with little expression or induction of *IFNL4, IFNA1, IFNG* or *IFNE*
191 (**Supplemental Figure 4A**). The kinetics of the expressed IFN genes all followed a similar
192 pattern, *i.e*., little induction was detected at 1 dpi, robust induction noted at 3 dpi, whereas
193 induction waned rapidly by 7 and 14 dpi (**Figure 3A**).
194

195 Using a previously defined Type I INF-stimulated gene (ISG) set, a robust ISG response was
196 observed that peaked at 3 dpi and waned thereafter (**Figure 3B**) (35). The ISGs remained
197 elevated over baseline in most cultures at 14 dpi. Notably, a small number of ISGs exhibited a
198 more persistent response, defined as greater fold changes over mock samples at 14 than 3 dpi.

199 These genes included *IFI27, BST2, IFI6*, and *IFI44L* (**Supplemental Figure 4B**). In contrast to
200 RNA data, a smaller number of ISGs were detected by proteomics of luminal secretions (**Figure**
201 **3C**). ISG proteins markedly increased in secretions at 3 dpi above 1 dpi levels, including
202 CXCL10, LAP3, and SAMHD1, whereas the majority of ISG proteins in luminal secretions
203 peaked at 7-14 dpi. This difference may represent a lag between ISG gene induction and protein
204 secretion and/or ISG release post-cell death.
205
206 To relate SARS-CoV-2 infection to IFN and ISG responses over the infection interval, we
207 plotted SARS-CoV-2 infection, IFN responses, and RNA-measured ISG responses as a function
208 of the percent peak mean response vs. time (**Figure 3D**). Compared to both viral titer and viral N
209 TPM (**Figure 3D, i and ii**), the intracellular IFN RNA responses peaked at 3 dpi, waned over 7-
210 14 dpi, and did not differ between viral titer suppressor vs. non-suppressor groups (**Figure**
211 **3Diii**). In comparison to IFN responses, the ISG responses exhibited similar kinetics at 3 dpi but
212 were persistently expressed over the experimental interval (**Figure 3Div**), again with no
213 significant differences between suppressor and non-suppressor cultures. These data are generally
214 consistent with the associations predicted for a SARS-CoV-2-induced IFN and subsequent ISG
215 response (41). Notably, the patterns of IFN and ISG responses were not directly related to the
216 detection of live infectious virus (titer) at 14 dpi as revealed by suppressor vs. non-suppressor
217 comparison. Thus, the persistent IFN and ISG responses could be driven by the continued
218 presence of intracellular viral RNA transcripts and/or epigenetic changes that prevent a quick
219 loss of IFN/ISG gene expression during a viral event.
220
221 **D. Global Transcriptomic Responses to SARS-CoV-2 Virus Infection 1-14 dpi.**

222 In addition to ISG responses, bulk RNAseq was used to catalogue other global epithelial
223 responses to SARS-CoV-2 infection with time. Principal component analyses (PCA) and
224 differential gene expression (DEG) analyses of the integrated HBE RNA expression dataset
225 demonstrated that virus treatment was a strong overall driver of major differences in HBE cell
226 gene expression post-infection at all timepoints measured (**Figure 4A-C**). SARS-CoV-2
227 infection induced significant up and down regulation of in gene expression, with different DEG
228 noted across time post-infection, especially after 1 dpi (**Figure 4, C and D, and Supplemental**
229 **Figure 5A**). A combined heatmap of differentially regulated genes comparing SARS-CoV-2-
230 infected vs. mock HBE cultures across all times and treatment groups provides visualization of
231 the major shifts driven by time (**Supplemental Figure 5B**).
232
233 As predicted from the large number of DEGs and the clustering data, pathway analyses identified
234 highly significant pathway signatures driven by SARS-CoV-2 infection (**Supplemental Table**
235 **2**). A simplified heatmap of pathway responses demonstrated several key processes significantly
236 altered at times from 1 to 14 dpi (**Figure 4E**). These pathways included interferon and cytokine
237 signaling, mitotic signaling, NOTCH/Wnt signaling, and several stress pathways, including
238 senescence and programmed cell death. Notably, no relationships were detected between IFs,
239 ISGs, or genes associated with infectious viral production (*e.g.*, viperin, tetherin) and suppressor
240 vs. non-suppressor status (data not shown). Down-regulated pathways at 7 dpi related to
241 translation could reflect the activity of ISGs to control viral infection.
242
243 We also asked if genes identified in GWAS studies (42) were involved in epithelial responses to
244 SARS-CoV-2 in HBE. Interestingly, many of the genes identified in GWAS studies associated

245 with Covid-19 susceptibility and/or severity were expressed in airway epithelia, and as a group,
246 they were responsive to virus infection after 3 dpi (**Supplemental Figure 5C**). These results
247 suggest that the epithelial response, not just immune cell responses, to virus infection could play
248 key roles in the presentation of Covid-19 in the clinic.
249
250 **E. Acute 1-3 dpi Cell Biologic Responses to Peak SARS-CoV-2 Infection of HBE Cultures**
251 We next sought to characterize the effects of SARS-CoV-2 infection on HBEs at peak titers (3
252 dpi) using a combination of morphologic, cell biologic, proteomics, mass spectroscopy, and bulk
253 RNAseq approaches. Previous studies have shown that the SARS-CoV-2 1-3 dpi interval is
254 associated with a high degree of shedding of infected and apoptotic/necrotic dead ciliated cells
255 (28). Cell death is also associated with release of cellular danger associated signals (DAMPs)
256 (30). Consistent with these data, an increased incidence of cell death was observed at 3 dpi as
257 indexed by the TUNEL assay (**Figure 5Ai and Supplemental Figure 6A**) and measures of
258 *ZBP1* RNA (**Supplemental Figure 6B**) (43). Mass spectrometric analyses of luminal secretions
259 revealed increased LDHB release over the 3-7 dpi interval (**Figure 5Aii**) and increased HMGB1
260 release that peaked at 3 dpi (44) (**Figure 5Aiii**).
261
262 Airway epithelia also manifest a complex balance of small molecule-mediated mechanisms that
263 can promote or dampen inflammatory responses to injury. We have previously reported that
264 release of ATP as a DAMP is coincident with peak SARS-CoV-2 infections of HBE cells and
265 serves as a second signal to promote inflammasome activation in locally resident airway
266 macrophages (15). ATP is metabolized on airways surfaces by a series of extracellular metabolic
267 enzymes that convert ATP to intermediate metabolites (AMP, adenosine, inosine, hypoxanthine,

268 xanthine) with a final product of uric acid (UAC) (**Supplemental Figure 6C**). Expression of
269 many genes within this pathway were altered in the 3-7 dpi interval (**Supplemental Figure 6Ci**),
270 and mass spectrometric analysis of HBE apical secretions revealed increases in ATP metabolites
271 and uric acid at day 3 dpi (**Figure 5Bi-ii and Supplemental Figure 6Cii**), consistent with acute
272 ATP release serving as a pro-inflammatory/pro-inflammasome-activating moiety.

273

274 Another small molecule pathway known to be regulated in relationship to viral infection is the
275 methionine salvage pathway, in which the anti-inflammatory molecule methylthioadenosine
276 (MTA) is converted back to methionine (45). We observed an increase in apical concentrations
277 of MTA with a corresponding decrease in adenine (a product of MTA hydrolysis) at day 3 dpi
278 with no significant change in methionine levels (**Figure 5Biii-iv**) in parallel with decreased
279 expression of genes involved in the methionine salvage pathway (**Supplemental Figure 6D**).
280 These findings suggest the virus-induced downregulation of this salvage pathway with
281 augmented MTA anti-inflammatory activity early in the post infection interval.

282

283 Bulk RNAseq analyses revealed additional global alterations in fundamental HBE cell biologic
284 functions associated with peak SARS-CoV-2 infection. For example, a large fraction of the
285 nuclear-encoded mitochondrial genes were suppressed at 3 dpi but were overexpressed later
286 (**Figure 5C**). A strong upregulation at 3 dpi of DNA methylation/chromatin remodeling
287 signatures, *e.g.*, histone acetylation, was also observed which was maintained but declined over
288 14 dpi (**Figure 5D**).

289

290 Inflammatory/cytokine genes included in the "cytokine-cytokine receptor interaction" KEGG

291 pathway (hsa04060) were also globally elevated by virus at 3 dpi and after (**Figure 5E**).
292 However, the genes in this pathway appeared to cluster in two broad categories, one that peaked
293 at 7 dpi and remained elevated and a second group that that were non-responsive to virus
294 infection.
295

296 **F. Adaptive, Maladaptive, and Reparative 3-14 dpi HBE Responses Post-Peak Viral SARS-**
297 **CoV-2 Infection**

298 In many airway disease states following injury, *e.g.*, virus infection, the epithelium remodels
299 from the ciliated cell-dominated state to one characterized by mucus cell metaplasia (46).
300 Accordingly, we characterized the cellular morphologies of HBE cultures over the post-SARS-
301 CoV-2 peak infectious interval to test for repair/metaplastic processes post-SARS-CoV-2
302 infection. While ciliated cell loss was not evident at 3 dpi, an ~ 50% reduction of ciliated cell
303 numbers in infected cultures was observed at 14 dpi compared to mock (**Figure 6Ai**). Further,
304 the ratio of ciliated cell gene expression to ciliated cell numbers differed between infected and
305 mock cultures, with lower numbers of ciliated cells present for equivalent ciliated cell gene
306 expression in the infected group (**Figure 6Aii**). A comprehensive heatmap of ciliated cell gene
307 expression shows high variability, but a general reduction in mature multi-ciliated cell gene
308 expression after virus infection was observed at 3 and 7 dpi (**Supplemental Figure 7A**). Newly
309 differentiating ciliated cells transition from suprabasal/secretory cells through a deuterosomal
310 cell state (47). Interestingly, despite an overall decrease in ciliated cells and ciliated cell gene
311 expression, HBE cultures post-virus exhibited an increase in deuterosomal cell gene expression,
312 especially at 7 dpi (**Figure 6Aiii and Supplemental Figure 7B**). These data suggest that there is
313 a delay/failure of the deuterosomal cell population to regenerate a mature multiciliated

314 epithelium.

315

316 Consistent with our previous report, AB-PAS staining demonstrated an increase in AB-PAS-
317 positive cells by 14 dpi, consistent with mucus cell metaplasia, in SARS-CoV-2-infected cultures
318 (**Supplemental Figure 7C** (46). Mucus cell metaplasia can reflect metaplasia of pre-existing
319 secretory cells into a mucus ("goblet") cell phenotype and/or commitment of regenerative cells,
320 *e.g.*, basal cells/suprabasal cells, into this cellular phenotype. Pertinent to these possibilities,
321 analyses of bulk RNAseq data revealed 1) an increase in basal cell and cell cycling genes (*e.g.*,
322 TP53 cell cycle pathway) in the interval post-peak infection, consistent with the notion that at
323 least part of the mucus cell metaplasia represented a cell proliferative/replacement response to
324 viral injury (**Figure 6B**); and 2) strong upregulation of EGFR signaling pathways that are likely
325 to mediate a component of the mucus metaplastic response to SARS-CoV-2 (46, 48, 49) (**Figure**
326 **6C)**.

327

328 The post-infection 7-14 dpi HBE epithelium also exhibited other indices of chronic
329 injury/damage. For example, upregulation of genes associated with cellular senescence at 3, 7
330 and 14 dpi was observed (**Supplemental Figure 7D**). Epithelial cells in the senescent state may
331 contribute to the pro-inflammatory pathways that persisted over the 14-d interval post-infection
332 (**Figure 5E**) (50). Adrenomedullin, which recruits ILC2s into airway walls and promotes Type 2
333 responses, was also upregulated in the post 3 dpi state (**Supplemental Figure 7E**) (51). In
334 parallel, there was a reduction in mitochondrial-encoded gene expression over the 7-14 dpi
335 interval, supporting the concept that virus infections lead to defects in cellular bioenergetics
336 (**Figure 6D**). The downregulation of mitochondrial-encoded genes contrasted to increased

337 expression of nuclear-encoded mitochondrial genes shown in **Figure 5C**. Thus, the post-SARS-
338 CoV-2-infected epithelium exhibits a complex spectrum of repair, adaptation, and dysfunction.
339

340 **G. Host Defense Responses to SARS-CoV-2-Infected Airway Epithelia**

341 In the context of injury, airway epithelia need to maintain elements of host defense. A major host
342 airway defense mechanism is the mucociliary transport system (52). This system is in part
343 dependent on ciliated cell numbers, which are reduced (see **Figure 6A**), predicting a degradation
344 of the efficiency of this system (53). However, mucociliary transport is also governed by the
345 mass of mucins on airway surfaces and the hydration of secreted mucins mediated by airway
346 epithelial ion transport systems (52, 54). An increase in the dominant host defense airway
347 epithelial secreted mucin, MUC5B, was observed by RNA, proteomics, and histologic
348 measurements, particularly at the 14 dpi interval post SARS-CoV-2 infection (**Figure 7A**).
349 *MUC5AC* was expressed basally at lower levels, its expression increased transiently with
350 infection, but the absolute RNA levels remained low compared to MUC5B (**Supplemental**
351 **Figure 8A**). Note that overall MUC5B RNA and protein levels, but not MUC5AC, correlated
352 well (**Supplemental Figure 8B**).
353

354 In parallel with increased mucin secretion, there was a significant upregulation at 7-14 dpi of a
355 broad class of ion transport genes that mediate fluid secretion (**Figure 7B**). A central pathway
356 mediating airway surface hydration includes the CFTR Cl^- channel and regulators of CFTR Cl^-
357 channel fluid secretory activity (55). Both CFTR gene expression and multiple regulatory
358 components of CFTR activity were upregulated. In contrast, key genes involved in fluid
359 absorption, *e.g.*, *SCNN1β* and *SCNN1γ*, were not upregulated and clustered separately in the

360 heatmap. The mucin and ion transport gene expression signatures suggest that airway surfaces
361 post-infection upregulate pathways to maintain/restore mucociliary transport by secretion of a
362 well-hydrated mucus to offset loss of ciliation and "flush" viruses/shed cells from airway
363 surfaces.
364
365 Finally, airway epithelia can respond to infection with increased synthesis and secretion of host
366 defense proteins and small molecules. While annotated antioxidant genes were variable in their
367 response post-infection (**Supplemental Figure 8C**), secreted antioxidant proteins were routinely
368 increased post-infection (**Figure 7C and Supplemental Figure 8D**). In contrast, proteomics
369 revealed a striking reduction in secretion of other host defense proteins, *e.g.*, SCGB1A1 (**Figure**
370 **7Di and Supplemental Figure 8E**), and the pathway for antimicrobial peptides (which includes
371 lysozyme, lactoferrin, SLPI, S100A8/9, and BPIFA/B1) was amongst the most downregulated
372 proteomic pathway signatures across the entire study (**Figure 7Dii and Supplemental Figure**
373 **8F)** (56). Notably, no relationships were detected between the suppressor/non-suppressor state at
374 the RNA or protein level for secreted proteins, with reported antiviral effects, including
375 lactotransferrin, BPIFA1, BPIFB1, SLIPI, or MUC5B/MUC5AC mucins (data not shown). At
376 the RNA-only level, no relationships were observed between the suppressor vs. non-suppressor
377 state and beta, defensins, nitric oxide synthesis 1, 2, or 3, and cathelicidin (data not shown).
378
379 **H. Comparison of Infection of HBE Cultures as a Function of the Sex of the Donor**
380 Note, because the sexes were not perfectly matched across batches in the 14 day protocol
381 (**Supplemental Figure 1A**), a batch correction was necessary, which confounded the sex
382 analyses (see **Supplemental Methods**). However, because, as described below, female sex was

383 found to produce higher viral titers in the 14 day protocol which could have dominated over
384 technical batch variables, the Protocol 1, 14 day studies were supplemented by data from a
385 replicate single-batch 3 day study (Protocol 2) focused on the effects of sex on infectivity from
386 0-3 dpi (**Supplemental Figure 1B**). Each protocol is discussed separately below.
387
388 In the 14 day protocol (Protocol 1), female donor HBE cultures exhibited a more rapid rise in
389 SARS-CoV-2 infection and higher peak levels of SARS-CoV-2 infection than cultures from
390 male donors as indexed by viral titers and secreted NCAP protein (**Figure 8, Ai and ii,**
391 **Supplemental Figure 9A**). In contrast, the mean rates of suppression of viral titer, N TPM, and
392 extracellular viral proteins were not different between females and males (**Figure 8A, iii and iv,**
393 **and Supplemental Figure 9A and B**). Differences in cilia, ACE2, TMPRSS2 and TMEM106B
394 were not evident between the sexes that would explain the increase viral titer in females at 3 dpi
395 (**Supplemental Figure 9, C and D**). No differences were observed in SARS-CoV-2 mutation
396 load as a function of sex (**Supplemental Figure 8E**).
397
398 To test for sex-dependent differences in host epithelial genes that might relate to sex-dependent
399 differential SARS-CoV-2 infectivity, global transcriptomic differences between male and female
400 mock cultures were evaluated to characterize the state of gene expression prior to infection.
401 Notably, very few differentially expressed genes were observed between male vs. female
402 cultures over the 1-14 dpi interval in the mock infected cultures (**Figure 8B**). Nearly all the
403 differentially expressed genes in the absence of infection (mock) between female and male
404 cultures reflected the sex chromosome genes (**Figure 8C**), and no pathways were consistently
405 different in male vs. female mock cultures across the four timepoints measured (**Figure 8D**). The

406 major difference between the sexes after virus infection were noticed as an increase in the
407 number of genes upregulated in females at 3 dpi (**Figure 8C**). Further evaluation of those genes
408 identified them as ISGs, which correlated with the increase in viral titer in females at 3 dpi.
409 These ISGs were not differentially regulated between male and female 14 dpi when viral titers
410 were not different. We conclude that in this study, male and female differences in the airway
411 epithelial transcriptome were extremely rare, dominated by X-Y chromosome-specific genes,
412 with no one expression profile predicting differences in infectivity.
413
414 Given the importance of possible sex differences in SARS-CoV-2 infectivity observed in the first
415 protocol, the acquisition phase of infection in HBE cultures was repeated for same donors but
416 infected as a single batch (**Supplemental Figure 1B**, Protocol 2). In the replication study, while
417 similar trends for females to show early increases in infectivity, at 1 dpi, no differences were
418 observed at 2 and 3 dpi (**Figure 8Ei**). Importantly, the combined data from the two studies
419 revealed no significant difference in infectivity between the sexes (**Figure 8Eii**). Thus, we
420 conclude there was little significant difference in sex-related SARS-CoV-2 infection of human
421 airway epithelia.
422
423 **I. SARS-CoV-2 Infection and repair of HBE cultures as a function of donor age:**
424 The 14 day two-batch protocol (Protocol 1) was matched for age. There were no differences in
425 the rate of acquisition of SARS-CoV-2 infection over the 0-3 dpi interval as a function of age as
426 reflected in titer, N TPM, or extracellular N (**Figure 9, Ai and E, and Supplemental Figure**
427 **10A**). Further, there were no consistent differences in resolution over that 3-14 dpi interval as a
428 function of donor age despite a tendency for young cultures to be more likely to suppress viral

429 titers (**Figure 9A, ii and iii, and Supplemental Figure 10, A and E**). No differences in viral
430 mutation load were observed across ages (**Supplemental Figure 10F**), nor were differences in
431 kinetics or magnitude of IFN gene responses, LDHB, or HMGB1 release detected
432 (**Supplemental Figure 10, B and C**). These data are different than a smaller *in vitro* nasal
433 epithelial study (57) but are consistent with age-dependent data from bronchial epithelia *in vitro*
434 (29, 58) and *in vivo* nasal SARS-CoV-2 RNA measures in the respiratory system (14).
435
436 The PCA plot of the mock HBE RNAseq transcriptomic data showed no clear separation as a
437 function of age, and surprisingly few differences in gene expression across age using our
438 filtering criteria were found (**Figure 9D and Supplemental Figure 10 D**). We then sought age-
439 dependent differences using pathway analyses in mock infected cultures across all timepoints
440 (**Figure 9C;** see **Supplemental Table 2** for access to analyses**)**. While each individual mock
441 timepoints comparison produced pathways that survived statistical significance testing, the
442 patterns were complex. A selected set of these pathways was chosen to depict major patterns
443 (**Figure 9C, D**). A consistent upregulation was noted across time in the young vs. mature
444 comparison in pathways that contained genes involved in cell cycle and DNA repair. Very few
445 pathways were consistently downregulated in young vs. mature, a notable exception being
446 biological oxidations. Overall, we conclude that the data supports the concept that cultures from
447 donors of all ages are surprisingly similar at the gene expression level, consistent with the
448 absence of age-dependent differences in infectivity in Protocol 1 and, indeed, the replication
449 protocol (Protocol 2) (**Figure 9E**).
450
451 Evaluation of age-dependent transcriptional responses to SARS-CoV-2 infection with respect to

452 epithelial damage and repair also yielded complex pathway responses with age across time post-
453 infection (**Figure 9D)**. Again, few consistent differences across age were noted across the entire
454 viral infection interval and ISG responses were similar across age groups (**Figure 9Fi**). The
455 tendency for cell cycle genes to be higher in young observed in mock cultures was maintained
456 after virus infection, except for 7 dpi where previous results show the highest cell cycling across
457 all ages (**Figure 6B**). In contrast, some of these genes were significantly downregulated in
458 elderly vs. mature after SARS-CoV-2 infection, indicating that the elderly may have reduced
459 capacity to cycle/repair after injury than young and mature cultures. The young donor cultures
460 also exhibited pathways indicating more robust DNA methylation (**Figure 9Fii**) with the elderly
461 showed reduced responses in these general pathways compared to the mature (or young) group.
462
463 In sum, we conclude that the respiratory epithelia of all ages exhibit similar baseline gene
464 expression properties and SARS-CoV-2 infectivity, but age-dependent differences in pathways
465 associated with repair were manifest.
466
467 **J. Variables related to abnormal airway repair at 14 dpi *in vitro*:**
468 The contributions of peak infection intensity (titer, TPM, NCAP) and epithelial damage (LDHB)
469 to a pathway-based index of failed epithelial repair (referred to as the repair index; see
470 **Supplemental Methods**) were tested. Surprisingly, no relationships between the intensity of
471 viral infection (**Figure 10A and Supplemental Figure 11, A and B**) and epithelial damage
472 (**LDHB; Figure 10B**) and the 14 dpi repair index were detected. Similarly, no relationships were
473 detected as a function of the sex of the donor (**Figure 10C**). In contrast, young age appeared to
474 be associated with an improved repair index (**Figure 10D**).

475

476 **K. Repair processes reflect *in vivo* COVID:**

477 We next asked whether genes that reflected failed return to a normal state, *i.e.*, failed repair, at 14
478 dpi in HBE cultures exhibited relevance to persistent long-COVID pulmonary disease. Analyses
479 of virus-infected vs. mock cultures identified 148 DEGs using an established threshold for
480 significance (see **Supplemental Methods**). We utilized this 14 dpi gene signature of "failed
481 repair" to query three datasets to address this question across two post-COVID lung disease
482 phenotypes.

483

484 We first analyzed spatial transcriptomics data from two cohorts with a post-COVID pulmonary
485 fibrosis phenotype. The first analysis focused on a reported autopsy study of 61 subjects ~ 30 d
486 post-SARS-CoV-2 symptom initiation with early pulmonary fibrotic histologic changes (46).
487 GSEA analyses revealed significant enrichment for the 14 dpi repair genes (e.g., *FCGBP,*
488 *MUC5B, SERPINA3, IFI27, CLXL1*) in persistently abnormal airway epithelia in this cohort
489 (**Figure 10E**). The second analysis focused on GeoMX spatial transcriptomics studies of
490 conducting airway epithelia of five subjects 6-12 mo post-initiation of SARS-CoV-2 symptoms
491 who exhibited persistent CT abnormalities and required video-assisted transthoracic surgery
492 (VATS) biopsies (**Supplemental Methods**). Histological evaluation of the biopsies revealed a
493 pulmonary fibrotic phenotype. Notably, the GSEA analysis again revealed significant enrichment
494 of the 14 dpi repair genes in diseased airway epithelial regions of the biopsied long-COVID
495 lungs (**Figure 10F**). Thus, the altered repair processes identified in 14 dpi HBE persist in the
496 airway regions of subjects with long-COVID pulmonary fibrotic phenotypes.

497

498 We next studied a long pulmonary COVID phenotype that manifests as chronic cough, sputum
499 production, and chest congestion. Recently, transbronchoscopic epithelial biopsies of subjects
500 exhibiting this phenotype persistently for ~ 18 mo post-SARS-CoV-2 infection vs. subjects who
501 resolved symptoms post-SARS-CoV-2 were reported (59). The 14 dpi HBE SARS-CoV-2 DEG
502 signature was enriched in the symptomatic as compared to non-symptomatic/control post-SARS-
503 CoV-2 infection groups, suggesting persistently abnormal repair contributes to the long-COVID
504 bronchitic phenotype **(Figure 10G**). A pathway analysis was performed on the gene set
505 representing failed repair. As predicted, the genes representing the ISG pathway were enriched
506 and correlated with the presence of viral transcripts (**Figure 10H**). Other upregulated pathways
507 in this gene set included neutrophil, complement, hypoxia, and interleukin signaling (**Figure**
508 **10I**).
509
510 **Discussion:**
511 The clinical outcomes of SARS-CoV-2 infections vary widely, reflecting a complex interplay
512 between the virus and host defense and reparative properties. This study explored potential age-
513 and sex-dependent contributions of respiratory epithelia to SARS-CoV-2 outcomes through 14
514 days post-infection. This study also offered the opportunity to investigate relationships between
515 *in vitro* intermediate-term repair (14 d) with long-term epithelial properties in subjects with long
516 COVID respiratory syndromes.
517
518 No differences in the rates of acquisition or peak viral titers, TPM, viral proteins, or viral
519 mutation load were consistently observed across cultures derived from children, mature adults, or
520 the elderly, consistent with previous reports of bronchial epithelia (29, 58). Key cell biologic

521 variables reported to govern infection rates also did not differ across age groups, including ACE2
522 expression, TMPRSS2 expression, culture ciliation, or kinetics/magnitude of IF responses, again
523 consistent with previous reports (29, 30, 60). RNA bulk-seq analyses of paired mock HBE
524 cultures prior to infection showed little differential gene expression in single genes across all
525 donor ages in PCA plots and DEG analyses. However, pathway analyses revealed an
526 upregulation in the young referenced to maturity of cell cycling and DNA repair pathways.
527
528 While all age groups exhibited similar epithelial morphology at d14, dominated by mucus
529 metaplasia, the younger subject cultures exhibited more robust cell cycling, DNA repair, and
530 oxidative stress pathway responses over the 3-14 dpi interval. Similar patterns of more
531 rapid/efficient repair have been observed in young vs. elderly subject cultures after a variety of
532 biologic and chemical insults (61), suggesting the young have in general more robust reparative
533 capacities in response to injury. The relatively consistent gene expression patterns observed after
534 virus across ages in these epithelial cultures suggest that immune cell function, not intrinsic
535 epithelial function, likely account for the age dependence of viral titer and severity outcomes
536 from SARS-CoV-2 infections (62-64). The childhood respiratory immune system has been
537 reported to be more versatile/trained to respond to a SARS-CoV-2 infection and prevent spread
538 to the lung with worsened clinical outcomes (13, 65-67). Conversely, a senescent immune
539 system has been posited to account for the worsened outcomes in the elderly (62, 63).
540
541 Regarding sex, our aggregate studies revealed no differences in SARS-CoV-2 infection in female
542 vs. male human bronchial epithelial cells, similar to a report of human nasal cultures in which no
543 differences in SARS-CoV-2 titer were detected as a function of sex (68). Epidemiologic studies

544 have clearly established that males, especially older males, exhibit more severe COVID-19
545 disease, but there is a paucity of large epidemiologic studies that have reported the differences in
546 titer in males vs. females *in vivo* (9). The two available studies described mixed findings, with a
547 small study of US Marine recruits reporting lower SARS-CoV-2 Ct values for males (9),
548 whereas a larger Saudi Arabian study reported a significantly lower Ct value in females of all
549 ages than males (62, 63).
550
551 The absence of a large effect of sex on SARS-CoV-2 epithelial infectivity is consistent with
552 analyses of female vs. male in mock (non-infected) cultures. PCA or DEG analyses of bulk-
553 RNAseq data revealed surprisingly few differences, limited to X and Y chromosomes, in
554 baseline gene expression, including ACE2 and TMPRSS2, between male and females (69). Note,
555 the Human Cell Atlas has released data describing multiple pulmonary epithelial cells as a
556 function of sex (70). Like our study, no differences in gene expression were observed, suggesting
557 human respiratory epithelia are not sex hormone responsive.
558
559 Combining the age and sex data into a larger dataset permitted insights into the airway epithelial
560 cell biologic response to the acute infection and repair processes. Aspects of the acute 3 dpi
561 response have been widely reported, including the selective infection of ciliated cells with
562 apoptotic and likely necrotic cell death (4, 28, 71, 72). The cell signaling processes during this
563 period are complex, with DAMP release, *e.g.*, HMGB1 and ATP, but also recruitment of anti-
564 inflammatory extra-cellular signals, *e.g.*, MTA. Major cell biologic responses at this peak period
565 also included suppression of mitochondrial and ribosomal gene expression. Coincident with
566 these responses were striking increases in expression of genes associated with histone acetylation

567 and inflammation. These responses reflect complex signaling cascades involving infected cells
568 and communication *in vivo* with immune/inflammatory cells via IF, DAMP, and inflammatory
569 mediators/cytokines.
570
571 Post-viral bacterial infections in the quasi-acute setting (wks) are common with respiratory
572 viruses in general, and severe COVID-19 subjects have an ~ 30% incidence of bacterial
573 superinfections (73). Many of these bacterial infections involve infection of airway mucus plugs
574 (46). Singanayagam et al., utilizing a rhinovirus challenge model in COPD subjects,
575 demonstrated that post-viral bacterial infections reflected neutrophil destruction of host airway
576 secretion antimicrobial substances and abnormal mucus production (74). Mucociliary clearance
577 is a key defense mechanism combating airway infection and exhibits a complex interplay
578 between ciliated cell numbers and mucus properties. Mucin secretion was upregulated, likely in
579 part due to EGFR and IL1R1 signaling, in SARS-CoV-2-infected HBE cultures (46). However,
580 mucins must be well hydrated to be transported effectively by MCC or the backup cough
581 mechanism. The upregulation of the dominant ion channel mediating fluid secretion, *i.e.*, CFTR,
582 coupled to an absence of upregulation of the channel that mediates opposing fluid absorption,
583 *i.e.*, ENaC, generates a scenario whereby newly secreted mucus is sufficiently hydrated to
584 mediate effective mucus clearance. However, the reduction post-SARS-CoV-2 infection in
585 ciliated cell numbers, with a concomitant loss of cilial force and mucus hydration
586 mechanosensing, can produce counterposing effects on MCC and cough clearance, particularly
587 in small airways, that produce mucus plugging in COVID lungs (46).
588
589 Infection of mucus plugs may be promoted by the absence of activities of antimicrobial

590 substances required for bacterial suppression on airway surfaces. In addition to neutrophil
591 cleavage of these substances post-viral infection, SARS-CoV-2 infection downregulated in
592 airway epithelia a complex of antimicrobial peptides, including CCSP, lactoferrin, and lysozyme
593 over the 3-14 dpi interval (74, 75). These molecules are key for suppressing bacterial growth
594 over intervals required for bacterial clearance by the MCC system, and the limitation of secreted
595 antimicrobial substances in the context of hampered MCC provides favorable conditions for
596 secondary airway bacterial infections (76).
597
598 Our study design allowed for detailed analyses of epithelial repair over 14 dpi in response to
599 SARS-CoV-2 infection. Airway epithelia emerged from peak infection into a phase at 7 dpi of
600 persistent but waning SARS-CoV-2 infection and repair/disrepair. By 14 dpi, airway epithelia
601 repaired via remodeling pathways that produced an abnormally mucus metaplastic, less ciliated
602 epithelium. This result likely is mediated in part by an increase in basal cell activation/cycling
603 and a skewing toward a mucus metaplastic phenotype due in part to increases in EGF ligand
604 production, *e.g.*, amphiregulin, and EFF-R signaling (48, 49). Our data describing the arrest of
605 ciliated cell maturation at the deuterosomal stage are consistent with this notion (40, 77). The
606 major variable identified in our study that associated with repair at 14 dpi was age, with young
607 repairing better, whereas no differences based on infection intensity or sex were detected.
608
609 Presumably, in most people post-SARS-CoV-2 infection, the epithelium continues to be repaired
610 over weeks *in vivo* with resolution of symptoms. However, a fraction of people post-SARS-CoV-
611 2 infection manifest "long pulmonary COVID" syndromes. Although multiple phenotypes are
612 reported associated with long pulmonary COVID, chronic bronchitic and pulmonary fibrotic

613 phenotypes are amongst the most common (59, 78-80). One mechanism that may contribute to
614 long-COVID pulmonary disease is the failure of infected pulmonary epithelia to repair. This
615 mechanism almost certainly contributes to the failure of infected alveolar AT2 cells to replenish
616 both AT2 and AT1 cells in long-COVID subjects with a resultant chronic fibrotic phenotype (81-
617 84).
618
619 Our data demonstrating the persistence of the HBE 14 dpi DEG signature in chronically diseased
620 airway epithelia in people with long-COVID fibrotic and bronchitic phenotypes suggest
621 persistent abnormal airway epithelial repair contributes to the pathogenesis of the airway
622 component of long-COVID pulmonary disease. Analyses of the pathways characterizing this
623 repair DEG set identified persistent ISG responses that correlated with the persistence of viral
624 transcripts in HBE cells at 14 dpi. It has been previously shown that chronically elevated ISG
625 expression in response to poly-IC exposure is associated with airway epithelial metaplasia,
626 similar to reports in alveolar epithelia (85, 86). One speculation that may describe persistent ISG
627 expression and airway metaplasia in some long-COVID individuals is a persistent low level of
628 non-infectious SARS-CoV-2 RNA expression in airway epithelial cells not cleared via
629 immunologic clearance mechanisms.
630
631 Our study has limitations. First, our study employed cultures of well-differentiated airway
632 epithelia. Whereas this design queries the intrinsic activity of the epithelium, it does not reprise
633 the activity of an epithelium *in vivo* exposed to the full spectrum of immune and stromal cells,
634 nor can it reflect the normal clearance of virus via immune cell activity. Thus, the culture
635 approach may have accounted for failure to identify key genes related to age-dependent host

636 antiviral defense *in vivo*. Second, our cultures were not exposed to media containing sex
637 hormones that may have been appropriate for sex. Third, the experimental sampling intervals
638 were not daily, making interpretation of rates of accumulation of virus/secreted proteins difficult.
639 Normalization was used to mitigate this problem. Fourth, while relatively large for a study in cell
640 culture, the study is expected to be underpowered to capture the entirety of the variability in the
641 human population.
642
643 In summary, our studies demonstrate that SARS-CoV-2 infection of airway epithelia leaves the
644 airway epithelium at 14 dpi in a repairing but complex state characterized by impaired mucus
645 transport, host defense protein secretion, and hyperinflammation. Young age, but neither sex nor
646 the peak intensity of the SARS-CoV-2 infection, modulates the post-viral repair state, consistent
647 with improved outcomes of the young (17, 26, 67, 87). The incomplete/abnormal repair state is
648 predicted to render the airway epithelium over a quasi-acute (days) post-infection interval
649 vulnerable to bacterial superinfections. The persistence of a failed repair state over the longer
650 term (months) may contribute to post-COVID pulmonary syndromes, including an airways
651 component of fibrotic sequelae and a bronchitic phenotype of cough and sputum production. A
652 persistent airway epithelial ISG response, possibly in response to poorly cleared viral RNA, may
653 be a driver of aspects of these long-COVID syndromes.
654
655
656 **Methods Section**
657 **A. Experimental Design for *In Vitro* Studies**
658 The experimental design is outlined in **Supplemental Figure 1**, with the technical details of each

659 individual assay provided in the **Supplement Material**. In broad terms, air–liquid interface
660 (ALI), well-differentiated HBE cultures were infected with SARS-CoV-2 and collected for
661 analyses as indicated (88). Cells were obtained under the protocol #03-1396 approved by the
662 University of North Carolina at Chapel Hill Biomedical Institutional Review Board in the
663 Marsico Lung Institute Tissue Procurement and Cell Culture Core. Three age groups were
664 studied: Young (age 0-8); Mature (age 21-29): Elderly (> 69). A replication protocol studied the
665 same donors in a single batch over a 3 dpi interval (**Supplemental Figure 1B**). Sample specifics
666 are provided in **Supplemental Table 1.** Key assays conducted consisted of titer, bulk RNAseq,
667 and proteomics from apical secretions. Key analyses included determination of differential gene
668 and protein expression (including pathway analyses), development of heatmaps, and an index to
669 describe disease repair. The index was tested against candidate variables hypothesized to govern
670 repair status, including infection intensity, sex, and donor age. Differences of means of outcome
671 measurements between experimental groups were tested with linear models, or in the case of
672 repeated measures design, with linear mixed-effect models. Analyses methods are provided in
673 detail in **Supplemental Material,** with details provided in figure legends as appropriate. Full
674 analyses of the results are provided in **Supplemental Files 1-24** with a description of those files
675 provided in **Supplemental Table 2**.
676

677 **Acknowledgments:** The authors wish to thank Eric Roe at the Marsico Lung Institute for expert
678 editorial and administrative assistance in the preparation of the manuscript. We also
679 acknowledge the University of North Carolina Pathology Services Core for providing
680 histological samples, especially the director of this core, Dr. Gabriela De la Cruz and her staff.
681

682 **Funding Statement:** The work is supported by National Institutes of Health grants P30
683 DK065988, R01 AI089728, and U19 AI116484; by Rapidly Emerging Antiviral Drug
684 Development Initiative (READDI) at the University of North Carolina at Chapel Hill,
685 appropriated by the North Carolina General Assembly; and by the Cystic Fibrosis Foundation
686 grants BOUCHE19R0, ESTHER24R0, and 00167G220 (Pickles).

687

688

689 **References**

690 1. Ellinghaus D, et al. Genomewide Association Study of Severe Covid-19 with Respiratory
691 Failure. *N Engl J Med.* 2020;383(16):1522-1534.
692 2. Kasela S, et al. Genetic and non-genetic factors affecting the expression of COVID-19-
693 relevant genes in the large airway epithelium. *Genome Med.* 2021;13(1):66.
694 3. Shelton JF, et al. The UGT2A1/UGT2A2 locus is associated with COVID-19-related loss
695 of smell or taste. *Nat Genet.* 2022;54(2):121-124.
696 4. Bridges JP, et al. Respiratory epithelial cell responses to SARS-CoV-2 in COVID-19.
697 *Thorax.* 2022;77(2):203-209.
698 5. Yang X, et al. Clinical course and outcomes of critically ill patients with SARS-CoV-2
699 pneumonia in Wuhan, China: a single-centered, retrospective, observational study.
700 *Lancet Respir Med.* 2020;8(5):475-481.
701 6. Hastie E, et al. Association between SARS-CoV-2 Viral Load and Patient Symptoms and
702 Clinical Outcomes Using Droplet Digital PCR. *Viruses.* 2023;15(2).

703 7. Jovanoski N, et al. Severity of COVID-19 and adverse long-term outcomes: a
704 retrospective cohort study based on a US electronic health record database. *BMJ Open.*
705 2021;11(12):e056284.
706 8. Pujadas E, et al. SARS-CoV-2 viral load predicts COVID-19 mortality. *Lancet Respir*
707 *Med.* 2020;8(9):e70.
708 9. Sauerwald N, et al. Pre-infection antiviral innate immunity contributes to sex differences
709 in SARS-CoV-2 infection. *Cell Syst.* 2022;13(11):924-931.e924.
710 10. Regis E, et al. Sex differences in innate anti-viral immune responses to respiratory
711 viruses and in their clinical outcomes in a birth cohort study. *Sci Rep.* 2021;11(1):23741.
712 11. Scully EP, et al. Considering how biological sex impacts immune responses and COVID-
713 19 outcomes. *Nat Rev Immunol.* 2020;20(7):442-447.
714 12. Ursin RL, Klein SL. Sex Differences in Respiratory Viral Pathogenesis and Treatments.
715 *Annu Rev Virol.* 2021;8(1):393-414.
716 13. O'Driscoll M, et al. Age-specific mortality and immunity patterns of SARS-CoV-2.
717 *Nature.* 2021;590(7844):140-145.
718 14. Koch CM, et al. Age-related Differences in the Nasal Mucosal Immune Response to
719 SARS-CoV-2. *Am J Respir Cell Mol Biol.* 2022;66(2):206-222.
720 15. Pierce CA, et al. COVID-19 and children. *Science.* 2022;377(6611):1144-1149.
721 16. Nakakubo S, et al. Associations of COVID-19 symptoms with omicron subvariants BA.2
722 and BA.5, host status, and clinical outcomes in Japan: a registry-based observational
723 study. *Lancet Infect Dis.* 2023;23(11):1244-1256.
724 17. Winkley K, et al. Immune cell residency in the nasal mucosa may partially explain
725 respiratory disease severity across the age range. *Sci Rep.* 2021;11(1):15927.

726 18. Nakanishi T, et al. Age-dependent impact of the major common genetic risk factor for
727 COVID-19 on severity and mortality. *J Clin Invest.* 2021;131(23).
728 19. Williamson EJ, et al. Factors associated with COVID-19-related death using
729 OpenSAFELY. *Nature.* 2020;584(7821):430-436.
730 20. Schneider JL, et al. The aging lung: Physiology, disease, and immunity. *Cell.*
731 2021;184(8):1990-2019.
732 21. Hao S, et al. Long-Term Modeling of SARS-CoV-2 Infection of In Vitro Cultured
733 Polarized Human Airway Epithelium. *mBio.* 2020;11(6).
734 22. Hou YJ, et al. SARS-CoV-2 Reverse Genetics Reveals a Variable Infection Gradient in
735 the Respiratory Tract. *Cell.* 2020;182(2):429-446.e414.
736 23. Killingley B, et al. Safety, tolerability and viral kinetics during SARS-CoV-2 human
737 challenge in young adults. *Nat Med.* 2022;28(5):1031-1041.
738 24. Kim D, et al. The Architecture of SARS-CoV-2 Transcriptome. *Cell.* 2020;181(4):914-
739 921.e910.
740 25. Walsh KA, et al. The duration of infectiousness of individuals infected with SARS-CoV-
741 2. *J Infect.* 2020;81(6):847-856.
742 26. Loske J, et al. Pre-activated antiviral innate immunity in the upper airways controls early
743 SARS-CoV-2 infection in children. *Nat Biotechnol.* 2022;40(3):319-324.
744 27. Hoffmann M, et al. SARS-CoV-2 Cell Entry Depends on ACE2 and TMPRSS2 and Is
745 Blocked by a Clinically Proven Protease Inhibitor. *Cell.* 2020;181(2):271-280.e278.
746 28. Morrison CB, et al. SARS-CoV-2 infection of airway cells causes intense viral and cell
747 shedding, two spreading mechanisms affected by IL-13. *Proc Natl Acad Sci U S A.*
748 2022;119(16):e2119680119.

749 29. Hysenaj L, et al. SARS-CoV-2 infection of airway organoids reveals conserved use of
750 Tetraspanin-8 by Ancestral, Delta, and Omicron variants. *Stem Cell Reports.*
751 2023;18(3):636-653.
752 30. Inde Z, et al. Age-dependent regulation of SARS-CoV-2 cell entry genes and cell death
753 programs correlates with COVID-19 severity. *Sci Adv.* 2021;7(34).
754 31. Buqaileh R, et al. Can cilia provide an entry gateway for SARS-CoV-2 to human ciliated
755 cells? *Physiol Genomics.* 2021;53(6):249-258.
756 32. Cheemarla NR, et al. Dynamic innate immune response determines susceptibility to
757 SARS-CoV-2 infection and early replication kinetics. *J Exp Med.* 2021;218(8).
758 33. Sungnak W, et al. SARS-CoV-2 entry factors are highly expressed in nasal epithelial
759 cells together with innate immune genes. *Nat Med.* 2020;26(5):681-687.
760 34. Ziegler CGK, et al. SARS-CoV-2 Receptor ACE2 Is an Interferon-Stimulated Gene in
761 Human Airway Epithelial Cells and Is Detected in Specific Cell Subsets across Tissues.
762 *Cell.* 2020;181(5):1016-1035.e1019.
763 35. Menachery VD, et al. Pathogenic influenza viruses and coronaviruses utilize similar and
764 contrasting approaches to control interferon-stimulated gene responses. *mBio.*
765 2014;5(3):e01174-01114.
766 36. Jackson CB, et al. Mechanisms of SARS-CoV-2 entry into cells. *Nat Rev Mol Cell Biol.*
767 2022;23(1):3-20.
768 37. Xu D, et al. PLSCR1 is a cell-autonomous defence factor against SARS-CoV-2 infection.
769 *Nature.* 2023;619(7971):819-827.
770 38. Blanco-Melo D, et al. Imbalanced Host Response to SARS-CoV-2 Drives Development
771 of COVID-19. *Cell.* 2020;181(5):1036-1045.e1039.

772 39. Broadbent L, et al. An endogenously activated antiviral state restricts SARS-CoV-2
773 infection in differentiated primary airway epithelial cells. *PLoS One.*
774 2022;17(4):e0266412.
775 40. Gamage AM, et al. Human Nasal Epithelial Cells Sustain Persistent SARS-CoV-2
776 Infection In Vitro, despite Eliciting a Prolonged Antiviral Response. *mBio.*
777 2022;13(1):e0343621.
778 41. Hatton CF, et al. Delayed induction of type I and III interferons mediates nasal epithelial
779 cell permissiveness to SARS-CoV-2. *Nat Commun.* 2021;12(1):7092.
780 42. COVID-19 Host Genetics Initiative. Mapping the human genetic architecture of COVID-
781 19. *Nature.* 2021;600(7889):472-477.
782 43. Li S, et al. SARS-CoV-2 Z-RNA activates the ZBP1-RIPK3 pathway to promote virus-
783 induced inflammatory responses. *Cell Res.* 2023;33(3):201-214.
784 44. Simpson J, et al. Respiratory Syncytial Virus Infection Promotes Necroptosis and
785 HMGB1 Release by Airway Epithelial Cells. *Am J Respir Crit Care Med.*
786 2020;201(11):1358-1371.
787 45. Chandler JD, Esther CR, Jr. Metabolomics of airways disease in cystic fibrosis. *Curr*
788 *Opin Pharmacol.* 2022;65:102238.
789 46. Kato T, et al. Prevalence and Mechanisms of Mucus Accumulation in COVID-19 Lung
790 Disease. *Am J Respir Crit Care Med.* 2022;206(11):1336-1352.
791 47. Lewis M, Stracker TH. Transcriptional regulation of multiciliated cell differentiation.
792 *Semin Cell Dev Biol.* 2021;110:51-60.

793 48. Venkataraman T, et al. Overactive Epidermal Growth Factor Receptor Signaling Leads to
794 Increased Fibrosis after Severe Acute Respiratory Syndrome Coronavirus Infection. *J*
795 *Virol.* 2017;91(12).
796 49. Venkataraman T, Frieman MB. The role of epidermal growth factor receptor (EGFR)
797 signaling in SARS coronavirus-induced pulmonary fibrosis. *Antiviral Res.* 2017;143:142-
798 150.
799 50. Coppé JP, et al. The senescence-associated secretory phenotype: the dark side of tumor
800 suppression. *Annu Rev Pathol.* 2010;5:99-118.
801 51. Han J, et al. Hypoxia induces adrenomedullin from lung epithelia, stimulating ILC2
802 inflammation and immunity. *J Exp Med.* 2022;219(6).
803 52. Hill DB, et al. Physiology and Pathophysiology of Human Airway Mucus. *Physiol Rev.*
804 2022;102(4):1757-1836.
805 53. Li Q, et al. Mucociliary transport deficiency and disease progression in Syrian hamsters
806 with SARS-CoV-2 infection. *JCI Insight.* 2023;8(1).
807 54. Boucher RC. Muco-Obstructive Lung Diseases. *N Engl J Med.* 2019;380(20):1941-1953.
808 55. Ghigo A, et al. Cell signaling and regulation of CFTR expression in cystic fibrosis cells
809 in the era of high efficiency modulator therapy. *J Cyst Fibros.* 2023;22 Suppl 1:S12-s16.
810 56. Akram KM, et al. An innate defense peptide BPIFA1/SPLUNC1 restricts influenza A
811 virus infection. *Mucosal Immunol.* 2018;11(1):71-81.
812 57. Woodall MNJ, et al. Age-specific nasal epithelial responses to SARS-CoV-2 infection.
813 *Nat Microbiol.* 2024;9(5):1293-1311.
814 58. Zhao C, et al. Activation of STAT3-mediated ciliated cell survival protects against severe
815 infection by respiratory syncytial virus. *J Clin Invest.* 2024;134(21).

816 59. Gerayeli FV, et al. Single-cell sequencing reveals cellular landscape alterations in the
817 airway mucosa of patients with pulmonary long COVID. *Eur Respir J.* 2024;64(5).
818 60. Tao Y, et al. Preliminary analyses of scRNA sequencing and immunohistochemistry of
819 children's lung tissues indicate the expression of SARS-CoV-2 entry-related genes may
820 not be the key reason for the milder syndromes of COVID-19 in children. *Clin Transl*
821 *Med.* 2021;11(5):e300.
822 61. Balázs A, et al. Age-Related Differences in Structure and Function of Nasal Epithelial
823 Cultures From Healthy Children and Elderly People. *Front Immunol.* 2022;13:822437.
824 62. Mahallawi WH, et al. Association of Viral Load in SARS-CoV-2 Patients With Age and
825 Gender. *Front Med (Lausanne).* 2021;8:608215.
826 63. Euser S, et al. SARS-CoV-2 viral-load distribution reveals that viral loads increase with
827 age: a retrospective cross-sectional cohort study. *Int J Epidemiol.* 2022;50(6):1795-1803.
828 64. Chua RL, et al. COVID-19 severity correlates with airway epithelium-immune cell
829 interactions identified by single-cell analysis. *Nat Biotechnol.* 2020;38(8):970-979.
830 65. Beer J, et al. Impaired immune response drives age-dependent severity of COVID-19. *J*
831 *Exp Med.* 2022;219(12).
832 66. Bartsch YC, et al. Humoral signatures of protective and pathological SARS-CoV-2
833 infection in children. *Nat Med.* 2021;27(3):454-462.
834 67. Yoshida M, et al. Local and systemic responses to SARS-CoV-2 infection in children and
835 adults. *Nature.* 2022;602(7896):321-327.
836 68. Brocke SA, et al. Woodsmoke particle exposure prior to SARS-CoV-2 infection alters
837 antiviral response gene expression in human nasal epithelial cells in a sex-dependent
838 manner. *Am J Physiol Lung Cell Mol Physiol.* 2022;322(3):L479-l494.

839 69. Silveyra P, et al. Sex and Gender Differences in Lung Disease. *Adv Exp Med Biol.*
840 2021;1304:227-258.
841 70. Sikkema L, et al. An integrated cell atlas of the lung in health and disease. *Nat Med.*
842 2023;29(6):1563-1577.
843 71. Robinot R, et al. SARS-CoV-2 infection induces the dedifferentiation of multiciliated
844 cells and impairs mucociliary clearance. *Nat Commun.* 2021;12(1):4354.
845 72. Zhu N, et al. Morphogenesis and cytopathic effect of SARS-CoV-2 infection in human
846 airway epithelial cells. *Nat Commun.* 2020;11(1):3910.
847 73. Huang C, et al. Clinical features of patients infected with 2019 novel coronavirus in
848 Wuhan, China. *Lancet.* 2020;395(10223):497-506.
849 74. Singanayagam A, et al. Airway mucins promote immunopathology in virus-exacerbated
850 chronic obstructive pulmonary disease. *J Clin Invest.* 2022;132(8):e120901.
851 75. McElvaney OF, et al. Protease-anti-protease compartmentalization in SARS-CoV-2
852 ARDS: Therapeutic implications. *EBioMedicine.* 2022;77:103894.
853 76. Ganz T. Antimicrobial polypeptides in host defense of the respiratory tract. *J Clin Invest.*
854 2002;109(6):693-697.
855 77. Wu K, et al. Lung Remodeling Regions in Long-Term Coronavirus Disease 2019 Feature
856 Basal Epithelial Cell Reprogramming. *Am J Pathol.* 2023.
857 78. Duong-Quy S, et al. Post-COVID-19 Pulmonary Fibrosis: Facts-Challenges and Futures:
858 A Narrative Review. *Pulm Ther.* 2023;9(3):295-307.
859 79. McGroder CF, et al. Pulmonary fibrosis 4 months after COVID-19 is associated with
860 severity of illness and blood leucocyte telomere length. *Thorax.* 2021;76(12):1242-1245.

861 80. Spagnolo P, et al. Pulmonary fibrosis secondary to COVID-19: a call to arms? *Lancet*
862 *Respir Med.* 2020;8(8):750-752.
863 81. Barkauskas CE, et al. Type 2 alveolar cells are stem cells in adult lung. *J Clin Invest.*
864 2013;123(7):3025-3036.
865 82. Strunz M, et al. Alveolar regeneration through a Krt8+ transitional stem cell state that
866 persists in human lung fibrosis. *Nat Commun.* 2020;11(1):3559.
867 83. Alysandratos KD, et al. Epithelial Stem and Progenitor Cells in Lung Repair and
868 Regeneration. *Annu Rev Physiol.* 2021;83:529-550.
869 84. Xie T, et al. Abnormal respiratory progenitors in fibrotic lung injury. *Stem Cell Res Ther.*
870 2022;13(1):64.
871 85. Onufer AP, et al. Influenza virus-induced type I interferons disrupt alveolar epithelial
872 repair and tight junction integrity in the developing lung. *Mucosal Immunol.* 2025.
873 86. Major J, et al. Type I and III interferons disrupt lung epithelial repair during recovery
874 from viral infection. *Science.* 2020;369(6504):712-717.
875 87. Freire PP, et al. The relationship between cytokine and neutrophil gene network
876 distinguishes SARS-CoV-2-infected patients by sex and age. *JCI Insight.* 2021;6(10).
877 88. Hou YJ, et al. SARS-CoV-2 D614G variant exhibits efficient replication ex vivo and
878 transmission in vivo. *Science.* 2020;370(6523):1464-1468.

879
880

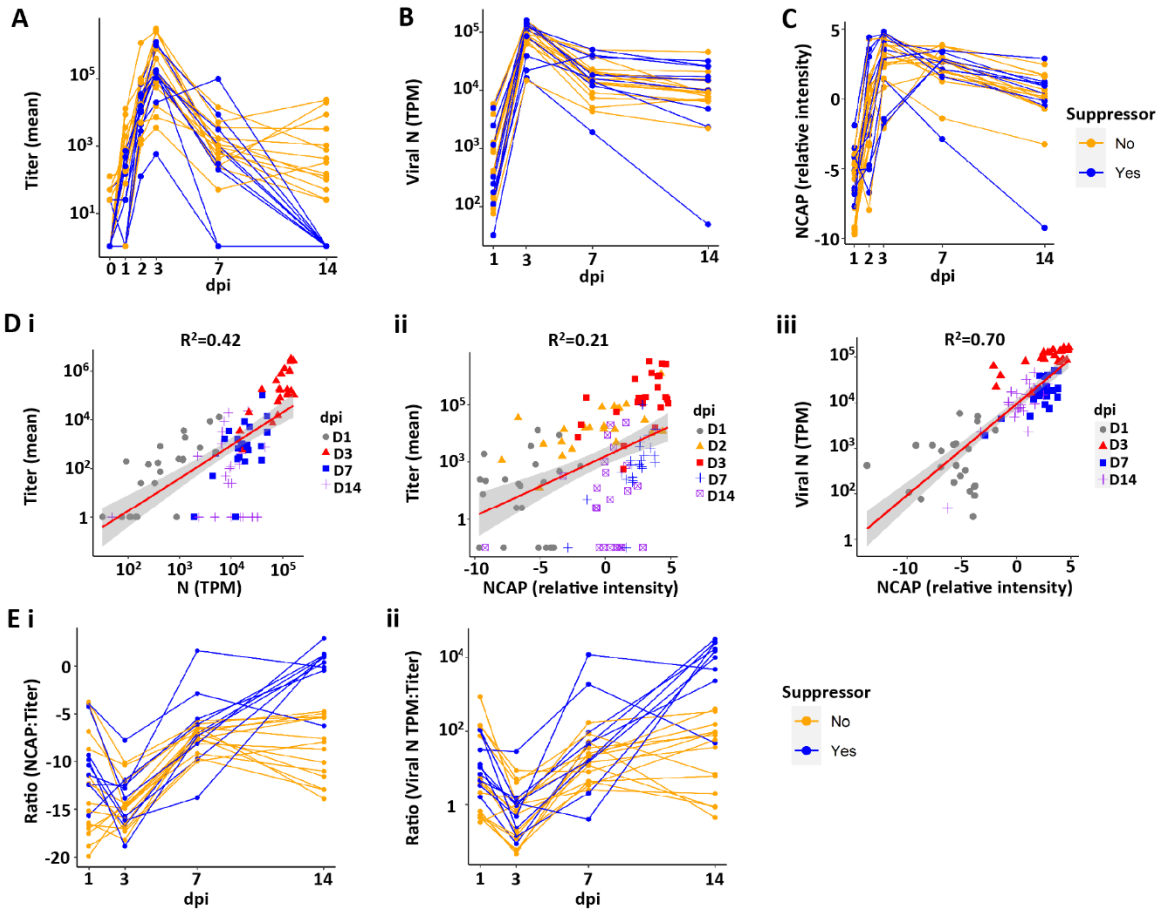

Figure 1. Indices of SARS-CoV-2 infection of all human bronchial epithelial (HBE) donor cultures with day post-infection (dpi). (A) SARS-CoV-2 titers over the 14 dpi interval, with each donor shown as connecting lines. HBE donor cultures that "suppressed" viral titers at d14 shown in blue. "Non-suppressors" are shown in orange. **(B)** Intracellular SARS-CoV-2 nucleoprotein (N) transcripts per million (TPM) by dpi for each donor culture. **(C)** Luminal extracellular viral NCAP protein by dpi for each donor. **(D)** Correlations between indices of SARS-CoV-2 infection. Shaded areas represent the 95% confidence interval. **(Di)** Correlation between viral titer and viral N TPM for each dpi. $p < 0.0001$. **(Dii)** Correlation between titer and nucleocapsid protein (NCAP) levels. $p < 0.0001$. Note that several 14 dpi samples are NCAP-positive and titer-negative. **(Diii)** Correlation between NCAP protein and SARS-CoV-2 viral N TPM for each dpi. $p < 0.0001$. Pearson correlation tests were used to calculate p-value and R^2. **(E)** Relationships between indices of SARS-CoV-2 infection with dpi. **(Ei)** Ratio of total intracellular viral TPM vs. titer by dpi. **(Eii)** Ratio of NCAP protein vs. titer by dpi.

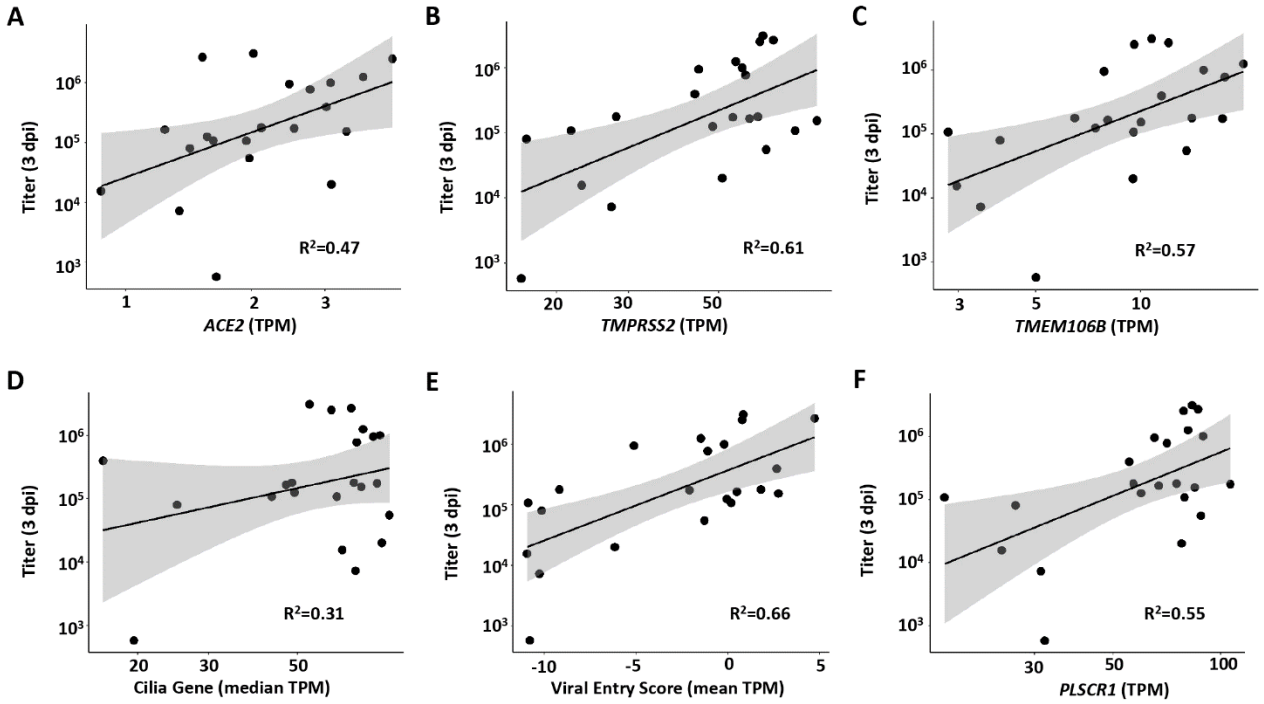

Figure 2. Host factor vs. peak viral titer relationships. Relationships between peak SARS-CoV-2 infection at 3 dpi and **(A)** long-form *ACE2* expression (p=0.24), **(B)** *TMPRSS2* expression (p=0.00249), **(C)** *TMEM106B* expression (p = 0.0049), **(D)** median cilia gene expression (p = 0.173), **(E)** HBE viral entry gene RNA score (p = 0.00071), and **(F)** *PLSCR1* expression (p = 0.0078). TPM=transcripts per million. All parameters listed on the X axes in A-F are measured from mock infected cultures at 1 dpi. Pearson correlation tests were used to calculate p-value and R^2. Shaded areas represent the 95% confidence intervals.

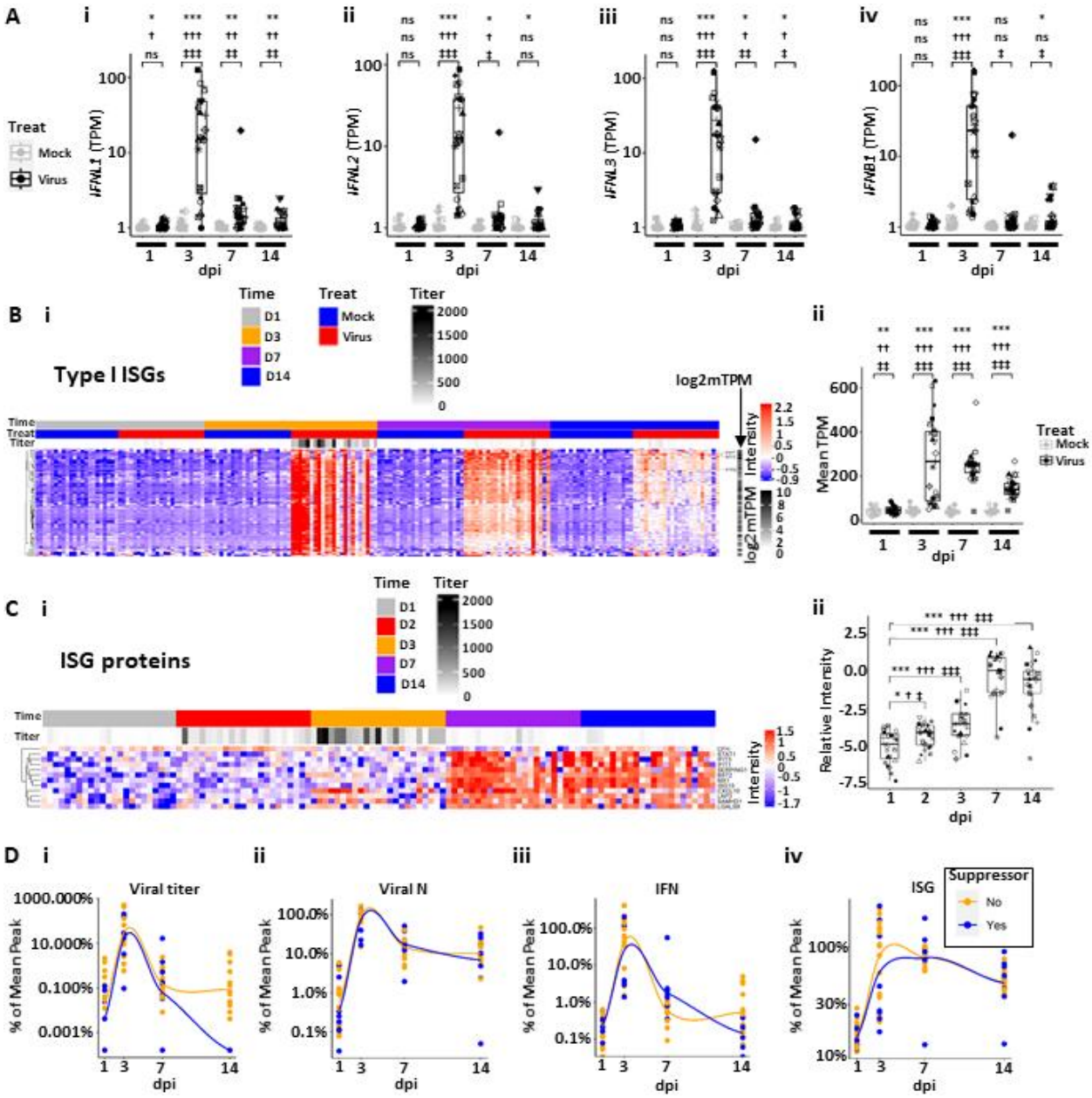

Figure 3. Interferon (IF) and interferon-stimulated gene (ISG) response kinetics to SARS-CoV-2 infection. (A) Box plots describing the expression values (in log10 scale plus offset of 1; TPM=transcripts per million) for HBE interferon responses over 14 dpi in mock and infected cultures for **(Ai)** *IFNL1,* **(Aii)** *IFNL2,* **(Aiii)** *IFNL3,* and (**Aiv**) *IFNB1***. (B)** HBE ISGs post-SARS-CoV-2 infection. **(Bi)** Heatmap describing pattern of ISG gene expression from 1-14 dpi. **(Bii)** Box plot describing level of mean ISG expression (TPM) for virus vs. mock from 1-14 dpi. **(C)** ISG proteins in luminal secretions from SARS-CoV-2-infected HBE cultures spanning 1-14 dpi. **(Ci)** Heatmap describing individual ISG proteins identified on HBE culture surfaces (normalized and imputed levels as described in methods). **(Cii)** Box plot describing mean level of secreted ISG protein for virus vs. mock from 1-14 dpi. **(D)** Relationships between viral infection, interferon (IFN), and ISG responses by dpi. Note, each parameter normalized to 100% mean peak response and depicted separately for HBE culture titer suppressors (blue) vs. non-suppressors (yellow). **(Di)** Mean percent of peak titers vs. dpi. **(Dii)** Mean percent nucleocapsid

(N) transcript levels vs. dpi. **(Diii)** Mean percent IFN responses vs. dpi. **(Div)** Mean percent ISG responses vs. dpi. Genes associated with the heatmap are listed in **Supplemental File 1.** Statistics utilized linear mixed models using tiered statistical testing: a) Univariate gene expression (TPM) by treatment (using symbol *; top row), b) Linear models with biological variables (age group + sex + median ciliated genes) and treatment (using symbol †; middle row), c) Linear models with biological and QC variables (age group + sex + median ciliated genes + batch + PC1) and treatment (most conservative, using symbol ‡; bottom row). The number of symbols represents statistical significance: ns = not significant; one symbol = $p<0.05$; two symbols = $p<0.01$, three symbols = $p<0.001$; four symbols = $p<0.0001$.

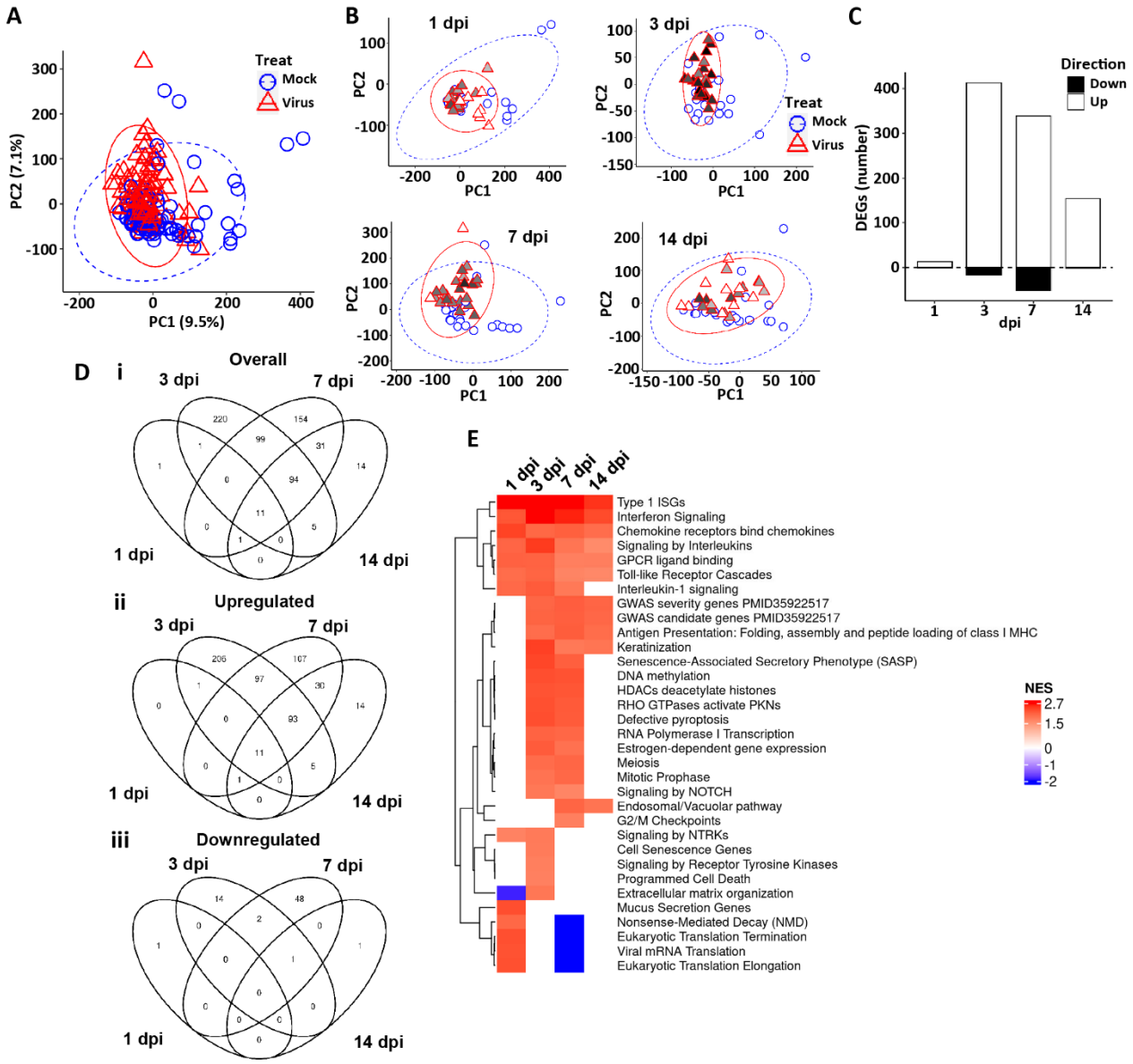

Figure 4. Global HBE responses to SARS-CoV-2 infection. **(A)** PCA plot representing the global bulk RNA transcriptome in mock and virus-infected cultures. All dpi are represented. **(B)** PCA plots representing global RNA transcriptome in mock and virus-infected cultures at the dpi indicated. In A and B, ellipses are drawn at 95% level assuming normal distributions of samples per group. PC=principal component. **(C)** Differentially expressed genes (DEGs) at the dpi indicated, showing number of regulated genes in both directions comparing virus-infected to mock treated cultures [(upregulated by SARS-CoV-2 in the upward bar (open); and downregulated in the downward bar (closed)]. DEGs represented are filtered at adjusted P-value of <0.05 and absolute log2 fold-change >1 with an average expression >0 (log2; or roughly TMP>1). **(D)** Venn diagrams depicting the overlap of DEGs between mock and SARS-CoV-2 infection across dpi groups. **(Di)** All DEGs; **(Dii)** DEGs upregulated by virus; **(Diii)** DEGs downregulated genes by virus. Filtering as in (C). **(E)** Heatmap of selected significant gene expression pathways identified as differentially expressed from the Reactome + custom pathway annotation set between virus infected vs. mock at indicated dpi. NES=normalized enrichment score. Red represents pathways upregulated by virus, blue represents pathways downregulated by virus.

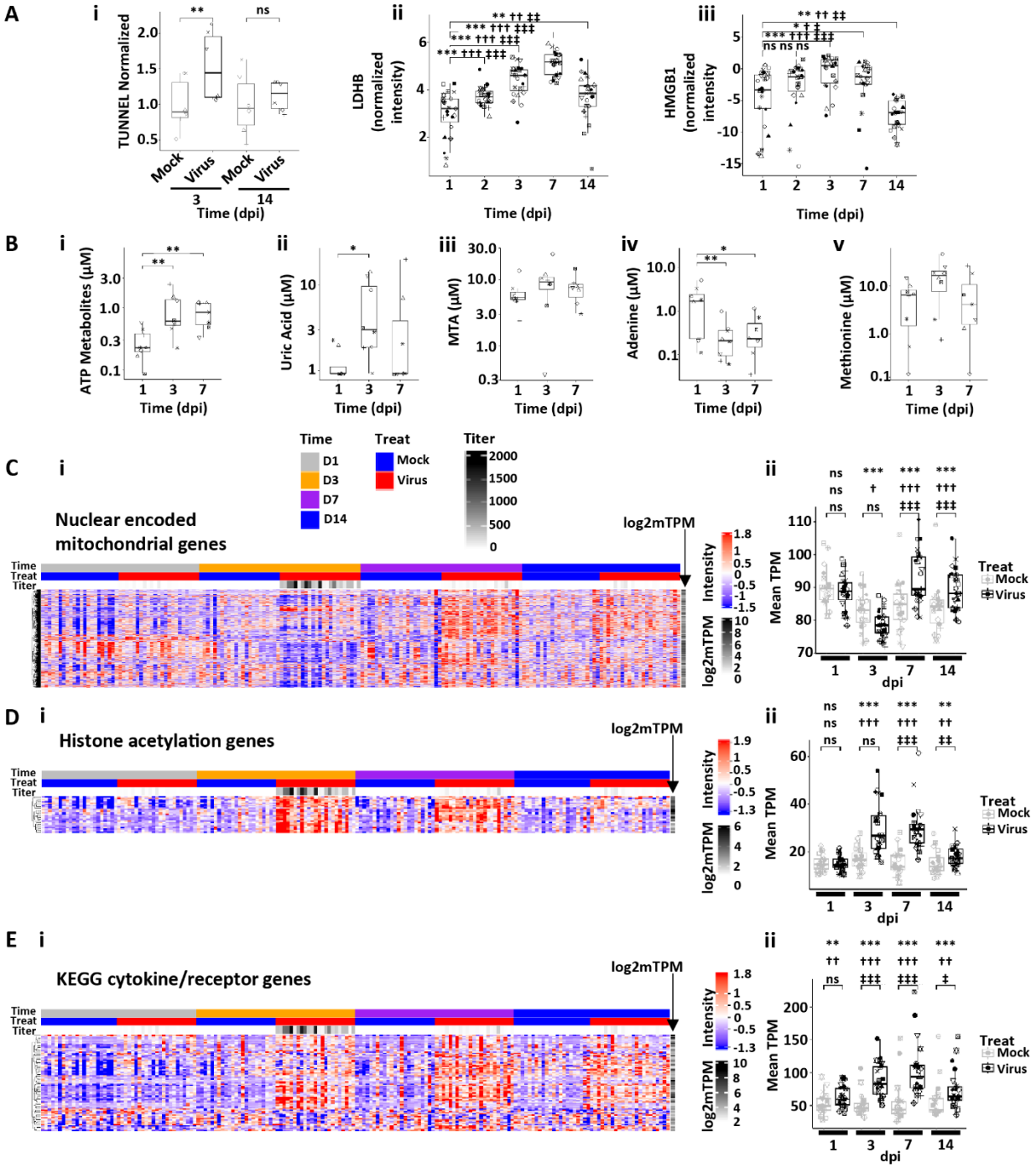

Figure 5. Human bronchial epithelial culture responses at peak SARS-CoV-2 infection. (A) Measures of cell death. **(Ai)** TUNEL assay quantification at 3 and 14 dpi in mock and infected cultures. ** = $p < 0.01$. **(Aii)** Box plots depicting LDHB release onto SARS-CoV-2-infected HBE culture surfaces spanning 1-14 dpi. **(Aiii)** Box plots depicting high mobility group box 1 (HMGB1) HBE apical surface protein levels spanning 1-14 dpi. **(B)** Measures of metabolites. Box plots depicting (**Bi**) total adenosine triphosphate (ATP) metabolites and (**Bii**) uric acid (UAC) concentrations, (**Biii**) MTA = methyl-thio-adenosine; (**Biv**) Ade = adenosine; and (**Bv**) Met = methionine as measured by mass spectroscopy in secretions at the indicated dpi. * = $p < 0.05$; **$p<0.01$. **(C-E)** Examples of pathway responses to peak

950 SARS-CpV-2 infection. **(Ci)** Heatmap of nuclear-encoded mitochondrial genes post-SARS-CoV-2 HBE
951 culture infection. **(Cii)** Box plots showing average gene expression per donor culture for mock and
952 SARS-CoV-2-infected cultures over dpi. **(Di)** Heatmap describing histone acetylation gene expression
953 over time post-SARS-CoV-2 infection. **(Dii)** Box plot describing average histone acetylation gene
954 expression levels per HBE culture donor for mock and SARS-CoV-2-infected cultures with time. **(Ei)**
955 Heatmap describing individual genes in the KEGG pathway for cytokines and receptors regulated by
956 SARS-CoV-2 infection over dpi. **(Eii)** Box plots showing average gene expression per HBE donor culture
957 for mock and SARS-CoV-2-infected cultures over dpi. Labels in Ci apply to all heatmaps. Statistics
958 conducted and symbols as described in **Figure 3** legend.
959

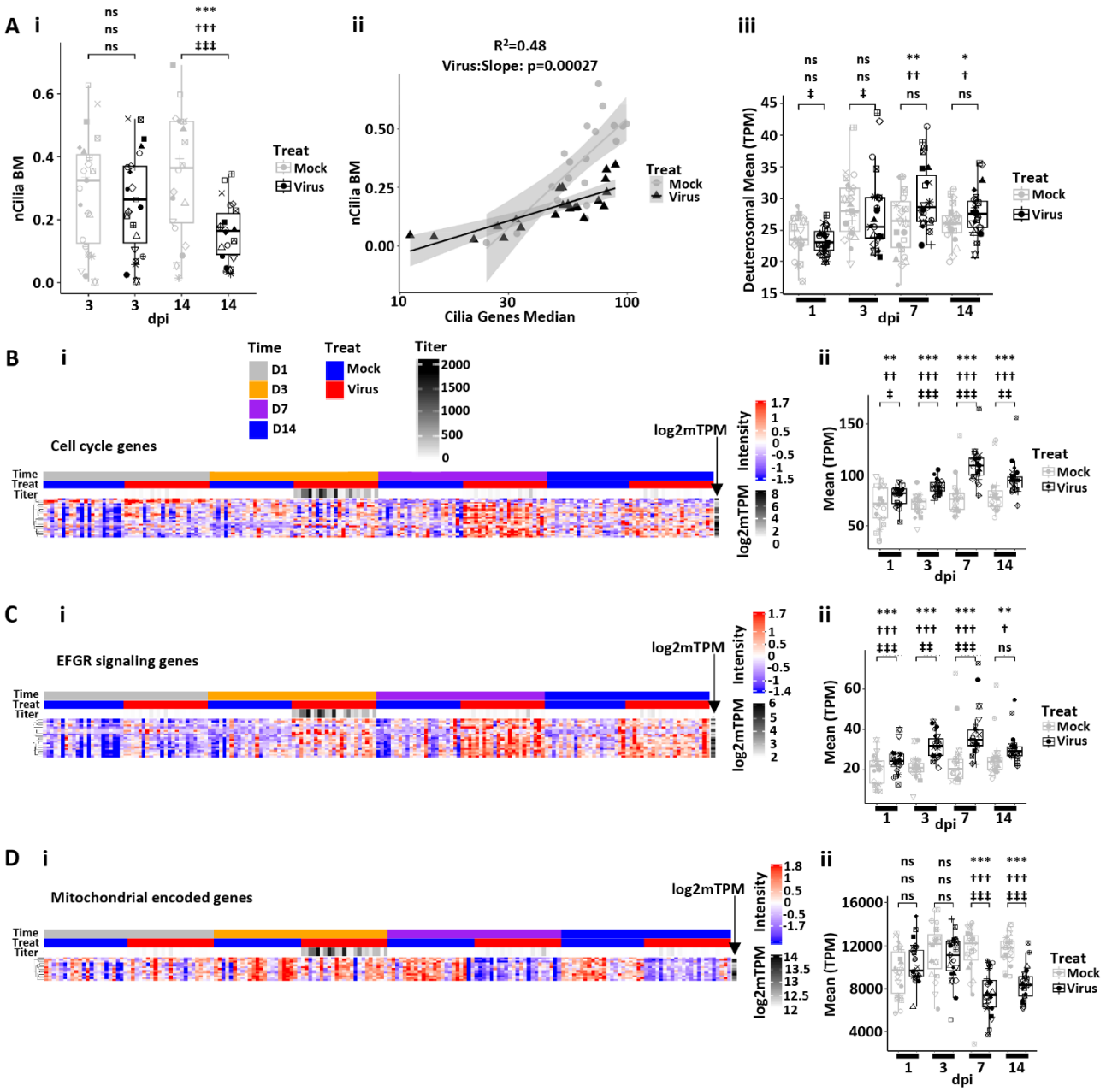

Figure 6. SARS-CoV-2-induced remodeling, senescence/inflammation, and repair in human bronchial epithelial cell cultures. (A) Ciliated cell quantification with infection. **(Ai)** Morphometric measurement of ciliation [cilia-covered apical surface/basement membrane (BM); measurement designated nCilia BM on axis label] for mock and SARS-CoV-2-infected HBE cultures at 3 and 14 dpi. **(Aii)** nCilia BM vs. median multi-ciliated cell gene expression pathway at 14 dpi. Mock HBE slope = 0.286 (SE 0.047), SARS-CoV-2-infected slope = 0.086 (SE 0.011) (delta = 0.176, SE = 0.043, $p < 0.00027$). Shaded areas represent the 95% confidence intervals. **(Aiii)** Mean deuterosomal cell gene expression for mock and SARS-CoV-2-infected cultures over dpi. **(B)** Cell cycling. **(Bi)** Heatmap depicting cell cycle gene expression over time post-infection. **(Bii)** Box plot depicting mean cell cycle gene expression (transcripts per million = TPM) over time post-infection. **(C)** EGFR signaling. **(Ci)** Heatmap depicting EGFR signaling genes as a function of time post-infection. **(Cii)** Box plots depicting mean EGFR signaling pathway gene expression over time post-infection. **(D)** Mitochondrial encoded

973 genes. **(Di)** Heatmap depicting mitochondrial encoded genes over time post-infection. **(Dii)** Box plot
974 depicting mean mitochondrial gene expression over time post-infection. Statistics conducted and symbols
975 as described in **Figure 3** legend. Headers in Bi apply to all heatmaps.
976

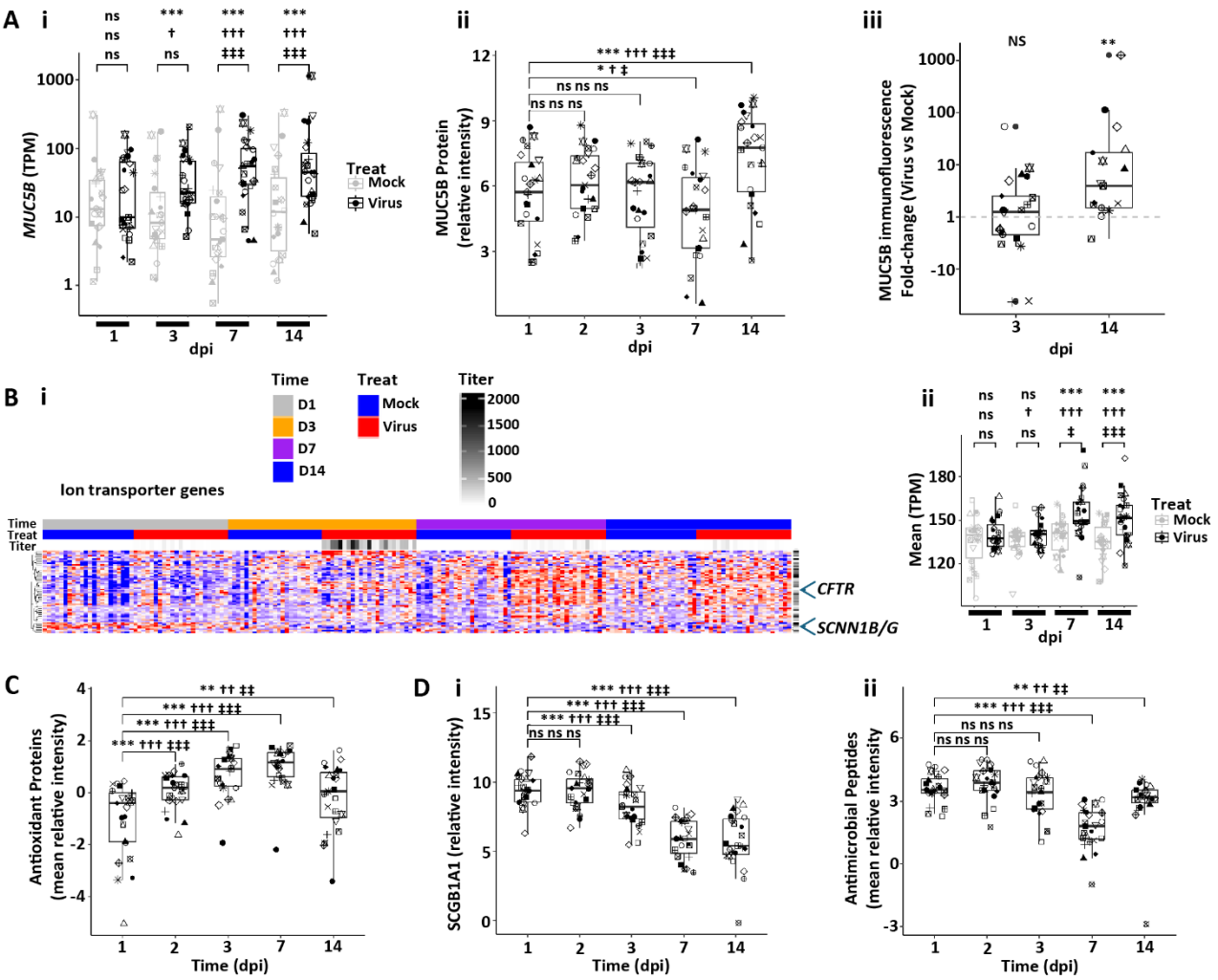

Figure 7. Human bronchial epithelial host mucosal defense responses to SARS-CoV-2 infection. (A) Secretory mucin expression. **(Ai)** Box plots depicting *MUC5B* RNA expression in mock vs. SARS-CoV-2-infected HBE cultures over dpi. **(Aii)** MUC5B protein secreted onto apical surfaces of mock vs. SARS-CoV-2-infected HBE cultures with time. **(Aiii)** Immunofluorescent MUC5B levels in SARS-CoV-2 ratioed to mock HBE culture levels at 3 and 14 dpi. **(B)** Ion transport genes. **(Bi)** Heatmap depicting pattern of ion transport genes in mock vs. SARS-CoV-2-infected HBE cultures with time post-infection. **(Bii)** Box plot depicting mean ion transport gene expression over time. **(C)** Box plot depicting mean antioxidant proteins collected from culture apical surfaces over time post-infection. **(D)** Antimicrobial defense molecules. (**Di**) Box plot depicting SCGB1A1 protein levels with time post infection. **(Dii)** Box plots depicting mean Reactome antimicrobial proteins with time post-infection. Statistics conducted and symbols as described in **Figure 3** legend.

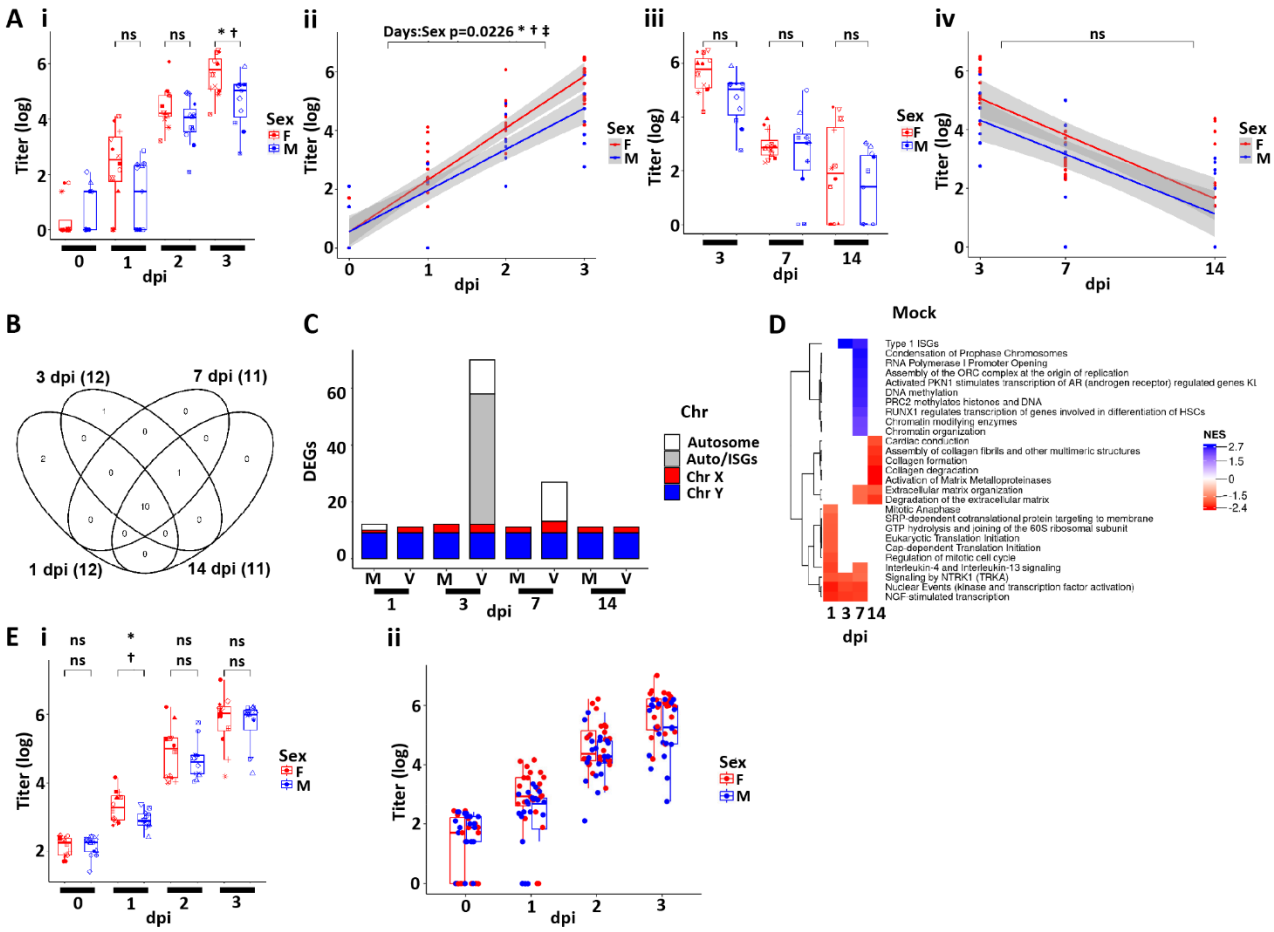

Figure 8. SARS-CoV-2 infectivity and HBE culture host responses as a function of sex. (A) Box plots depicting mean titers in SARS-CoV-2 infected HBE cultures from 0-3 dpi colored by sex. **(Aii)** Slopes of mean titers in each sex for dpi 0-3 (slope = 1.77 for females and 1.40 for males). The p-value of the difference between the slopes (-0.37) is 0.0226. The shaded areas represent the 95% confidence intervals. **(Aiii/iv)** As for (Ai-iii) expect representing titer data for dpi 3, 7, and 14. **(B)** Venn diagram representing differentially expressed genes (DEGs) between sexes from analyses of mock HBE cultures at the dpi indicated. Numbers in parentheses represent the total number of DEGs in each group. DEGs represented are filtered at adjusted P-value of <0.05 and absolute log2 fold-change >1 with an average expression >0 (log2; or roughly TMP>1). **(C)** Schematic representation of DEGs between the two sexes at the times and treatments indicated (m=mock; v=virus). Coloring represents the location of the DEGs on the chromosomes where Auto=all autosomes. DEGs represented are filtered as for (B). **(D)** Simplified heatmap of differentially expressed pathways from Reactome + custom annotation set for female vs. male in mock infected HBE cultures. Red pathways are upregulated in females compared to males; blue pathways are upregulated in males compared to females. NES=normalized enrichment score. **(E)** Replication cohort (Protocol 2). **(Ei)** Box plots depicting mean titers in SARS-CoV-2 infected HBE cultures from 0-3 dpi colored by sex Protocol 2. **(Eii)** Combined titer data for Protocols 1-2. No significant difference between sexes were found for any timepoint measured.

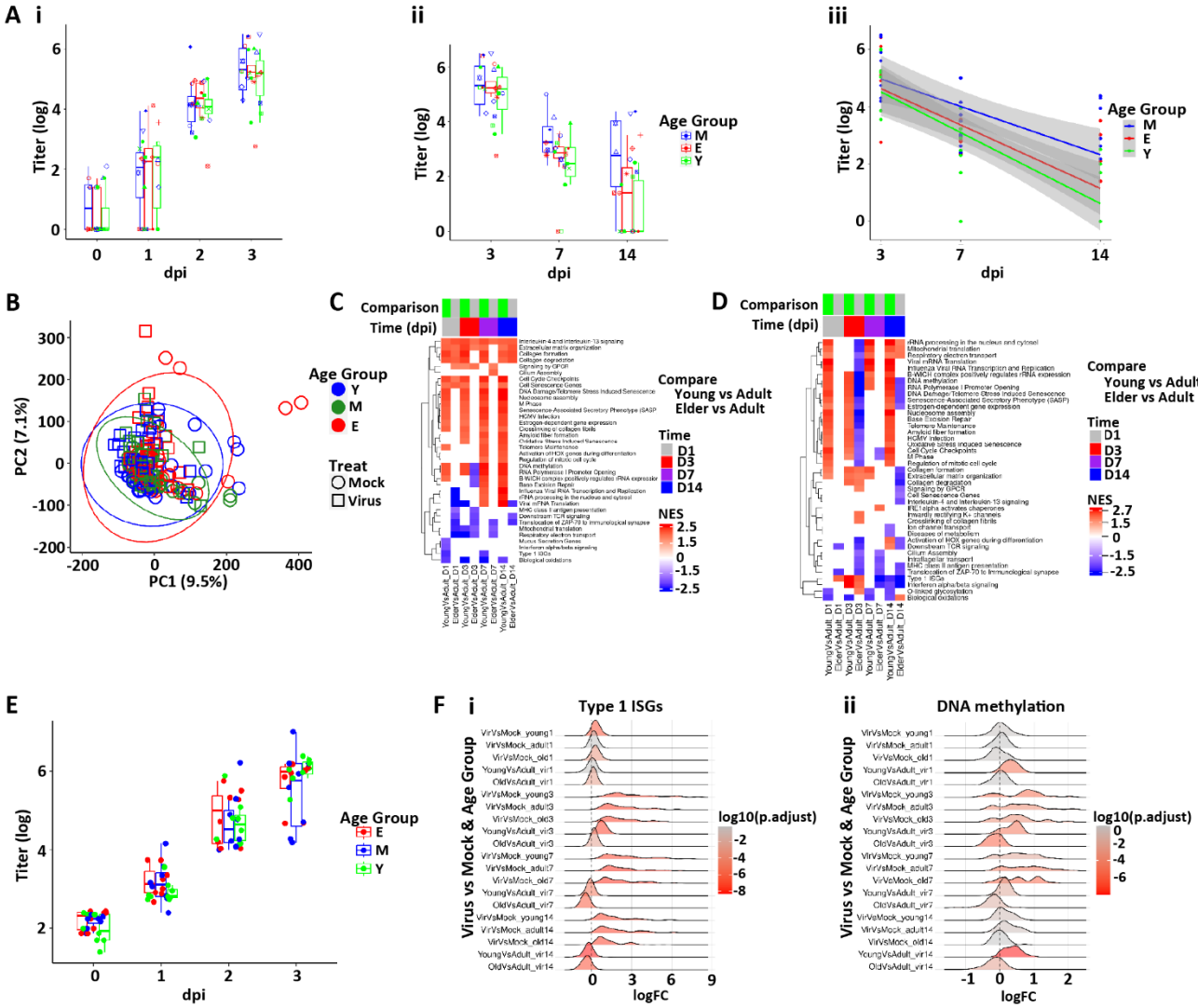

Figure 9. SARS-CoV-2 infectivity and HBE culture host responses as a function of age. (A) Box plots depicting mean titers in SARS-CoV-2 infected cultures separated into age groups. No significant differences were found among ages at any timepoint measured. **(Ai)** Titers 1-3 dpi; **(Aii)** titers 3-14 dpi. **(Aiii)** Slopes of viral titers from 3, 7, and 14 dpi as a function of age. M = mature; Y = young; E = elderly. Shaded areas represent the 95% confidence intervals. **(B)** PCA of global bulk RNAseq transcriptomics colored by age group. Ellipses are drawn at 95% level assuming normal distributions of samples per group. **(C)** Pathways selected from bulk RNAseq data by the Reactome + custom pathway annotation describing differentially regulated pathways in mock treated cultures between the age groups shown at the dpi indicated. **(D)** Selected differentially regulated pathways in virus-treated samples between the age groups shown at the indicated. For (C-D), NES=normalized enrichment score. **(E)** Replication Protocol 2 data for titer plotted by age. **(F)** Ridge plots representing **(Fi)** ISGs and **(Fii)** DNA methylation signatures between age groups and times dpi.

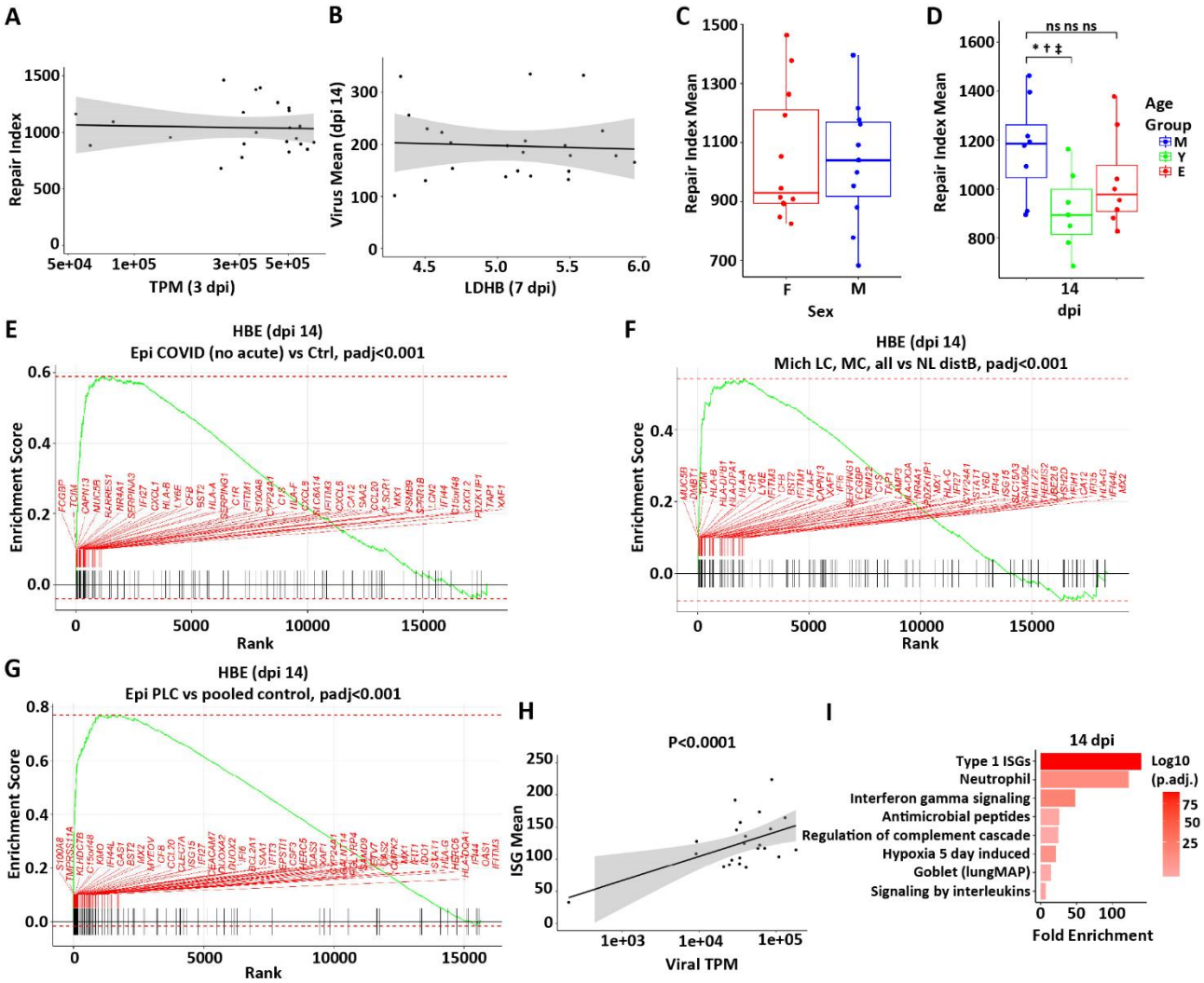

Figure 10. Relationship of failed repair to COVID-19 disease. A repair index score as a function of **(A)** viral gene expression (TPM) at 3 dpi, **(B)** peak LDHB protein in secretions at 7 dpi, **(C)** sex, and **(D)** age. All comparisons depict the repair index at 14 dpi. **(E-G)** Failed repair genes are enriched in GSEA analyses for **(E)** a reported autopsy (~ 30 d post-SARS-CoV-2 symptom initiation) with early pulmonary fibrotic histologic changes (46); **(F)** GeoMX spatial transcriptomics studies of conducting airway epithelia of five subjects 6-12 mo post-initiation of SARS-CoV-2 symptoms who exhibited persistent CT abnormalities and required VATS biopsies, again with fibrotic changes evident on histology; and **(G)** transbronchoscopic epithelial biopsies of subjects exhibiting a long pulmonary COVID phenotype that manifests as chronic cough, sputum production, and chest congestion persistently for ~ 18 mo post-SARS-CoV-2 infection vs. subjects who resolved symptoms post-SARS-CoV-2 (46). **(H)** Relationship between ISGs and viral TPM at 14 dpi (slope=0.68 SE 0.14, p<0.0001). **(I)** Selected pathways over-represented (enriched) in failed repair gene set. Shaded areas in A, B, and H represent the 95% confidence intervals.